

FAUST XX. The chemical structure and temperature profile of the IRAS 4A2 hot corino at 20-50 au

J. Frediani^{1,2,3}, M. De Simone^{2,4}, L. Testi^{1,4}, L. Podio⁴, C. Codella⁴, C. J. Chandler⁵, C. Ceccarelli⁶, L. Loinard^{7,8,9}, A. López-Sepulcre^{6,10}, B. Svoboda⁵, N. Sakai¹¹, L. Chahine⁶, Y. Aikawa¹², E. Bianchi⁴, M. Bouvier¹³, L. Cacciapuoti², P. Caselli¹⁴, S. B. Charnley¹⁵, I. Jimenez-Serra¹⁶, D. Johnstone^{17,18}, G. Sabatini⁴, Y. Shirley¹⁹, and S. Yamamoto²⁰

¹ DIFA, Dipartimento di Fisica e Astronomia, Università degli Studi di Bologna, Via Gobetti 93/2, I-40129 Bologna, Italy
e-mail: jenny.frediani@astro.su.se

² ESO, Karl Schwarzschild Str. 2, 85748 Garching bei München, Germany
e-mail: marta.desimone@eso.org

³ Department of Astronomy, Stockholm University, AlbaNova University Centre, 106 91 Stockholm, Sweden

⁴ INAF, Osservatorio Astrofisico di Arcetri, Largo E. Fermi 5, 50125 Firenze, Italy

⁵ National Radio Astronomy Observatory, 1011 Lopezville Rd, Socorro, NM 87801, USA

⁶ Univ. Grenoble Alpes, CNRS, IPAG, 38000 Grenoble, France

⁷ Instituto de Radioastronomía y Astrofísica, Universidad Nacional Autónoma de México, A.P. 3-72 (Xangari), 8701, Morelia, Mexico

⁸ Black Hole Initiative at Harvard University, 20 Garden Street, Cambridge, MA 02138, USA

⁹ David Rockefeller Center for Latin American Studies, Harvard University, 1730 Cambridge Street, Cambridge, MA 02138, USA

¹⁰ Institut de Radioastronomie Millimétrique (IRAM), 300 rue de la Piscine, 38406 Saint-Martin-d'Hères, France

¹¹ The Institute of Physical and Chemical Research (RIKEN), 2-1, Hirosawa, Wako-shi, Saitama 351-0198, Japan

¹² Department of Astronomy, The University of Tokyo, Bunkyo-ku, Tokyo 113-0033, Japan

¹³ Leiden Observatory, Leiden University, P.O. Box 9513, 23000 RA Leiden, The Netherlands

¹⁴ Center for Astrochemical Studies, Max-Planck-Institut für Extraterrestrische Physik, Gießenbachstraße 1, 85748 Garching, Germany

¹⁵ Astrochemistry Laboratory, Code 691, NASA Goddard Space Flight Center, 8800 Greenbelt Road, Greenbelt, MD 20771, USA

¹⁶ Centro de Astrobiología (CAB), INTA-CSIC, Carretera de Ajalvir km 4, Torrejón de Ardoz, 28850 Madrid, Spain

¹⁷ NRC Herzberg Astronomy and Astrophysics, 5071 West Saanich Road, Victoria, BC, V9E 2E7, Canada

¹⁸ Department of Physics and Astronomy, University of Victoria, Victoria, BC, V8P 5C2, Canada

¹⁹ Steward Observatory, 933 N Cherry Ave., Tucson, AZ 85721 USA

²⁰ The Graduate University for Advanced Studies (SOKENDAI), Shonan Village, Hayama, Kanagawa 240-0193, Japan

February 3, 2025

ABSTRACT

Context. Young low-mass protostars often possess hot corinos, compact, hot and dense regions bright in interstellar Complex Organic Molecules (iCOMs). Besides of their prebiotic role, iCOMs can be used as a powerful tool to characterize the chemical and physical properties of hot corinos.

Aims. Using ALMA/FAUST data we aim to explore the iCOMs emission at < 50 au scale around the Class 0 prototypical hot corino IRAS 4A2.

Methods. We imaged IRAS 4A2 in six abundant, common iCOMs (CH₃OH, HCOOCH₃, CH₃CHO, CH₃CH₂OH, CH₂OHCHO, and NH₂CHO), and derived their emitting size. The column density and gas temperature for each species were derived at 1 σ from a multi-line analysis by applying a non-LTE approach for CH₃OH, and LTE population or rotational diagram analysis for the other iCOMs. Thanks to the unique estimates of the absorption from foreground millimeter dust toward IRAS 4A2, we derived for the first time unbiased gas temperatures and column densities.

Results. We resolved the IRAS 4A2 hot corino finding evidence for a chemical spatial distribution in the inner 50 au, with the outer emitting radius increasing from ~ 22-23 au for NH₂CHO and CH₂OHCHO, followed by CH₃CH₂OH (~ 27 au), CH₃CHO (~ 28 au), HCOOCH₃ (~ 36 au), and out to ~ 40 au for CH₃OH. Combining our estimate of the gas temperature probed by each iCOM with their beam-deconvolved emission sizes, we inferred the gas temperature profile of the hot corino on scales of 20-50 au in radius, finding a power-law index q of approximately -1.

Conclusions. We observed, for the first time, a chemical segregation in iCOMs of the IRAS 4A2 hot corino, and derived the gas temperature profile of its inner envelope. The derived profile is steeper than when considering a simple spherical collapsing and optically-thin envelope, hinting at a partially optically-thick envelope or a gravitationally unstable disk-like structure.

Key words. astrochemistry – ISM: molecules – stars: formation - individual object: IRAS 4A2

arXiv:2501.19188v1 [astro-ph.EP] 31 Jan 2025

1. Introduction

Observations of Class II protostars, \sim Myr old stars with disks, and cosmochemical evidence from our Solar System suggest a rapid evolution of solids into planetary cores, followed by planet formation and disk-planet interaction earlier than originally thought (Johansen et al. 2014; Manara et al. 2018; Bernabò et al. 2022). While deriving accurate properties of younger Class 0/I disks ($\sim 10^{4-5}$ yr; Lada 1987; André et al. 2000; André 2002) is prone to very large uncertainties (Tung et al. 2024), numerical simulations suggest that they may harbour already the conditions required for planet formation (Lebreuilly et al. 2021, 2024). Some observations, albeit affected by large uncertainties, seem to support such a claim (Sheehan & Eisner 2018; Tychoniec et al. 2020). Therefore, a chemical characterization of the early Class 0/I stages is crucial to understand what a forming planet can inherit (Caselli & Ceccarelli 2012; Öberg & Bergin 2021; Ceccarelli et al. 2023).

Solar-type Class 0/I sources often possess compact (< 100 au), hot ($T > 100$ K), and dense ($n_{\text{H}} > 10^7 \text{ cm}^{-3}$) regions, named “hot corinos” (Ceccarelli 2004). These sources show high gas-phase abundances of interstellar Complex Organic Molecules (iCOMs, saturated C-bearing molecules with at least six atoms and including heteroatoms, such as N and O; Herbst & van Dishoeck 2009; Ceccarelli et al. 2017), liberated through the sublimation of the dust icy mantles (Ceccarelli 2023). The work by Maury et al. (2014) was pivotal in showing with interferometric observations the hot corino nature of IRAS 2A, where various iCOMs sizes were estimated to be much more compact than the beam size. In fact, due to their compactness, only four hot corinos have been spatially resolved so far: SVS13-A (Bianchi et al. 2022), HH212 (Lee et al. 2022), IRAS 16293-2422 A (Maureira et al. 2022), and B335 (Okoda et al. 2022). In these sources, the iCOMs are either spatially segregated within the resolved structure, or associated with accretion shocks/hot spots. However, for only a few of these chemical species a good physical characterization has been performed.

IRAS 4A2, the second discovered hot corino source, has an estimated size of about 70 au (from previous unresolved observations; Bottinelli et al. 2004; Taquet et al. 2015; López-Sepulcre et al. 2017; De Simone et al. 2017, 2020a). It is located in the nearby Perseus/NGC 1333 star forming region (~ 300 pc; Zucker et al. 2018; Ortiz-León et al. 2018), and is part of a binary system together with IRAS 4A1, ($1''8$, or ~ 540 au, away), with a total bolometric luminosity of $9.1 L_{\odot}$ (Kristensen et al. 2012; Karska et al. 2013). The system exhibits extended (4000 au) molecular outflow cavities, and evidence for a disk wind at 100 au scale (De Simone et al. 2020b, 2024; Chahine et al. 2024).

With this work, we use the iCOMs emission to characterize the inner 50 au of the IRAS 4A2 hot corino as part of the ALMA (Atacama Large sub-Millimeter Array)¹ Large Program (LP) FAUST (Fifty AU Study of the chemistry in the disc/envelope system of solar-like protostars; Codella et al. 2021).

The paper is organized as follows. In Sect. 2 are described the ALMA/FAUST observations, and the line identification of a sample of iCOMs detected toward IRAS 4A2. Section 3 presents our results. We first resolve the iCOMs molecular emission in the hot corino, and retrieve the spatial distribution of the different species (Sect. 3.1). Then we derive gas temperatures and column densities with both LTE and non-LTE methods (Sect. 3.2). In Sect. 4 we discuss the impact of dust continuum emission on the fitted quantities (4.1), and then directly derive a gas temperature profile at 50 au scales (4.2). The conclusions are wrapped

up in Sect. 5. In the appendix can be found, in order of reference in the text, the individual line spectra (Fig. A.1 to Fig. A.6), their spectral parameters and fit results (Tab. A.1), the results from image plane fitting of chosen lines (Tab. B.1), as well as complementary figures (Fig. B.1 and Fig. B.2). There are also dedicated appendices to the adopted methodology for the retrieval of physical parameters from the iCOMs lines (App. C and App. D), as well as supplementary material for the results and the discussion (App. E).

2. Observations and line identification

The observations of IRAS 4A we present here are part of the ALMA Large Program FAUST (PI. S. Yamamoto, 2018.1.01205.L) performed between October 2018 and September 2019 with baselines for the 12-m array from 15.1m to 3.6 km. Bandpass, flux, and phase calibrators are J0237+2848, J0336+3218 and J0328+3139, respectively. The map phase center is at R.A. (J2000) = $03^{\text{h}}29^{\text{m}}10^{\text{s}}.539$, and Dec. (J2000) = $+31^{\circ}13'30''.92$. We used the wide-band spectral windows at 230 GHz (Setup 1, hereafter S1), and at 240 GHz (Setup 2, hereafter S2), both with 1875 MHz bandwidth and 1.1 MHz ($\sim 1.4 \text{ km s}^{-1}$) of spectral resolution (Codella et al. 2021). The data were calibrated using the ALMA calibration pipeline in the Common Astronomy Software Applications package (CASA)², with an additional calibration routine to correct for the T_{sys} normalization issue³. Phase and amplitude self-calibration were performed on the continuum, generated using manually detected line-free continuum channels and applied to the cube (Chandler et al. in prep.). We cleaned and imaged the continuum-subtracted line cubes with CASA (V6.5.6) using a `briggs` weighting (`robust` = 0.5), multiscale deconvolution (`scales` = [0, 5, 15, 30, 60]), and `automasking`. The resulting synthesized beams are $0''.21 \times 0''.14$ ($\text{PA} = -3^{\circ}$) for S1, and $0''.17 \times 0''.12$ ($\text{PA} = -28^{\circ}$) for S2. We then primary beam corrected the cubes. The 7m ACA data are available only for S2, where we estimated a flux loss of about 25% over $0''.6$. For consistency, we proceeded analyzing the 12m configuration data alone for both setups. The absolute flux error is $\sim 20\%$, which includes the calibration uncertainty and an additional error for the spectral baseline determination.

We extracted the spectrum obtained using each of the two setups in the IRAS 4A2 dust continuum emission peak position: R.A. (J2000) = $3^{\text{h}}29^{\text{m}}10^{\text{s}}.431$ and Dec. (J2000) $+31^{\circ}13'32''.00$. (Fig. 1). We searched for the most abundant iCOMs, using the Cube Analysis and Rendering Tool for Astronomy package (CARTA; V4.0.0)⁴, namely methanol (CH_3OH), methyl formate (HCOOCH_3 , or CH_3OCHO ; hereafter we will use the former nomenclature), acetaldehyde (CH_3CHO), formamide (NH_2CHO), ethanol ($\text{CH}_3\text{CH}_2\text{OH}$, or $\text{C}_2\text{H}_5\text{OH}$; afterwards we will use the former nomenclature), and glycolaldehyde (CH_2OHCHO). We identified the lines manually using the CDMS (Müller et al. 2005) and JPL (Pickett et al. 1998) catalogs, verifying that all predicted transitions of the queried molecule were detected. We consider a detection if the signal-to-noise ratio is above 5. In total we detected 74 emission lines (see Tab. A.1): 9 of CH_3OH ($E_{\text{u}}=61-537$ K), 24 of HCOOCH_3 ($E_{\text{u}}=114-354$ K), 5 of CH_3CHO ($E_{\text{u}}=96-487$ K), 19 of $\text{CH}_3\text{CH}_2\text{OH}$ ($E_{\text{u}}=78-437$ K), 6 of NH_2CHO ($E_{\text{u}}=78-115$ K),

² <https://casa.nrao.edu>

³ <https://help.almascience.org/kb/articles/what-error-s-could-originate-from-the-correlator-spectral-normalization-and-tsys-calibration>

⁴ <https://cartavis.org>

¹ <https://www.almaobservatory.org/en/home/>

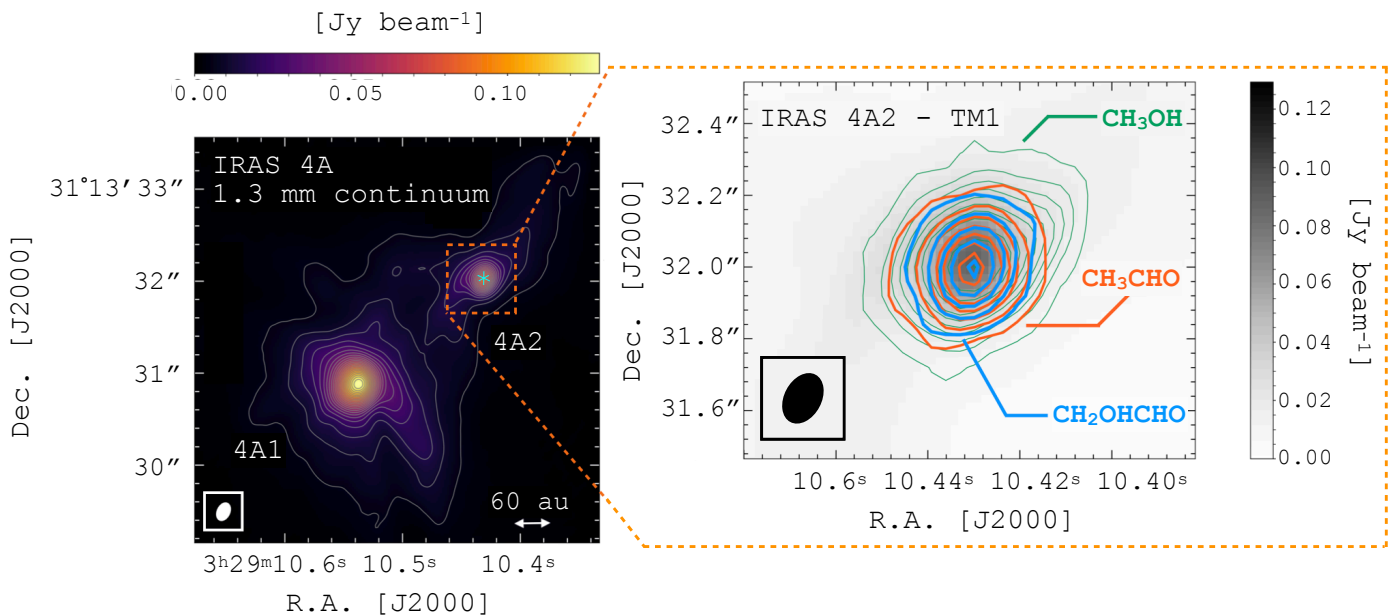


Fig. 1. Dust continuum and emission of selected iCOMs transitions towards IRAS 4A2. *Left:* 1.3 mm dust continuum emission in colour scale and grey contours. First contours and steps are 3σ ($\sigma = 0.6$ mJy beam⁻¹). The cyan star marks the IRAS 4A2 dust peak, $3^{\text{h}}29^{\text{m}}10^{\text{s}}.431$ (R.A.) and $+31^{\circ}13'32''00$ (Dec.). The beam is $0''.20 \times 0''.14$ (-26°). *Right:* Dust continuum (gray scale) overlaid with moment 0 contours maps of CH₃OH $16_{(-2,15)}-15_{(-3,13)}$ E (green), integrated over $+3$ to $+10$ km s⁻¹, CH₃CHO $13_{(0,13)}-12_{(0,12)}$ E [$v_t=2$] (orange), integrated over $+4$ to $+9$ km s⁻¹, and CH₂OHCHO $34_{(5,30)}-34_{(4,31)}$ (blue), integrated over $+6$ to $+8$ km s⁻¹. First contours and steps are 3 and 6σ respectively, with $\sigma = 3.7$ mJy beam⁻¹ km s⁻¹ for CH₃OH, $\sigma = 2.7$ mJy beam⁻¹ km s⁻¹ for CH₃CHO, and $\sigma = 2.3$ mJy beam⁻¹ km s⁻¹ for CH₂OHCHO. The beam is $0''.17 \times 0''.12$ (-28°).

and 11 of CH₂OHCHO ($E_u=242-489$ K), where E_u is the transition upper-state energy.

3. Results

3.1. Spatial segregation of iCOMs

To study the spatial distribution of the identified iCOMs, we produced and compared integrated intensity maps of different species using isolated transitions with similar E_u , so as to avoid excitation biases. Figure 1 shows, on the left, the IRAS 4A system in 1.3 mm dust continuum emission, and, on the right, a zoom-in of the same map onto IRAS 4A2, with over-plotted colored contours of the integrated intensity maps of three selected iCOMs transitions: CH₃OH $16_{(-2,15)}-15_{(-3,13)}$ E ($E_u=338$ K); CH₃CHO $13_{(0,13)}-12_{(0,12)}$ E ($E_u=461$ K); CH₂OHCHO $34_{(5,30)}-34_{(4,31)}$ ($E_u=344$ K). The moment 0 maps of all the isolated transitions for each species are in Fig. B.2. These maps show that the various iCOMs trace different scales. To quantify this, we estimated the emitting radius associated with each species by performing a 2D Gaussian fit of the emission on the integrated intensity maps using the `imfit` task in CASA. For the few transitions whose emission is clearly associated with IRAS 4A2 only, avoiding any contamination from the companion IRAS 4A1, we also performed a Gaussian fit on the visibility plane with the `uvmodelfit` task in CASA. Since the fit results in the visibility plane are consistent within $\pm 1-2$ au with the image plane determinations, we analyzed all the isolated lines using only the image plane results (Tab. B.1). Some examples of the fitted images and of the residual maps are in Fig. B.1. For all transitions, the residual maps of the fit show no emission above $2-3\sigma$. From the beam-deconvolved major (θ_M) and minor (θ_m) diameters of the fitted Gaussian ellipses (Tab. B.1), we derived a radius of the emitting line as half of the geometric average of θ_M and θ_m .

Figure 2 shows the beam-deconvolved radius (in au) for each isolated transition versus the line E_u . The iCOMs display differ-

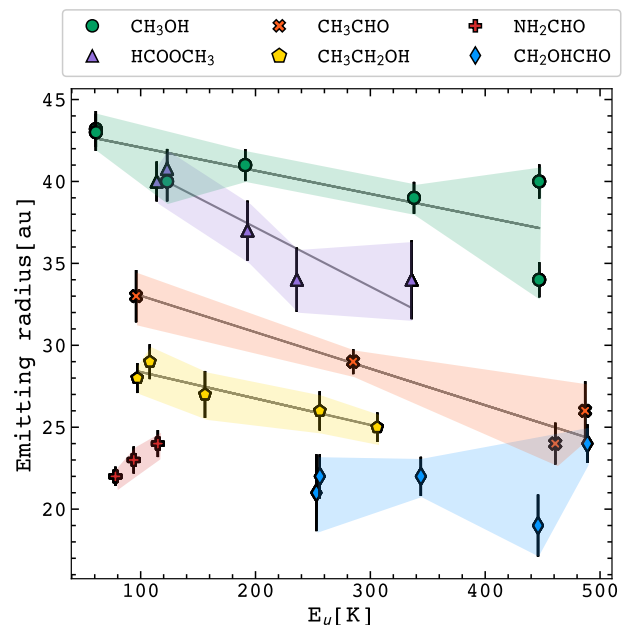


Fig. 2. iCOMs beam-deconvolved radius as a function of the line upper-state energy. The coloured markers correspond to a chosen sample (see Sect. 3.1 and Fig. B.2) of imaged and fitted iCOMs transitions. The grey solid lines indicate the linear fit performed on the derived radius. The shaded colored regions highlight the emitting regions associated with each iCOM.

ent emitting sizes, in other words, the observed transitions must trace a different outer radius in the hot corino, where the line optical depth is equal to or larger than 1. Therefore, the estimated emitting radii within error bars (shaded regions in Fig. 2) indicate that we are probing different regions of the hot corino of IRAS 4A2, extending out to an outer radius which spans be-

tween 16 and 40 au, depending on the considered species. We note, however, that the exact geometry of this molecular emission cannot be unambiguously determined with a 2D Gaussian fit. A higher angular resolution coupled with a detailed chemophysical model of the molecular line emission are needed to resolve this ambiguity. To estimate the dependence of the emitting size versus the transition, we linearly fitted the derived radius with respect to E_u , except for CH_2OHCHO and NH_2CHO due to their partially unresolved emission. The fit shows a small variation of the size as a function of E_u , with negative slopes deviating from zero by factors 0.014 ± 0.003 (CH_3OH , $\tilde{\chi}^2 = 4.7$), 0.04 ± 0.01 (HCOOCH_3 , $\tilde{\chi}^2 = 1.0$), $0.010 \pm 0.0022 \pm 0.005$ (CH_3CHO , $\tilde{\chi}^2 = 1.4$), and 0.016 ± 0.005 ($\text{CH}_3\text{CH}_2\text{OH}$; $\tilde{\chi}^2 = 0.4$). We therefore computed a weighted average emission region radius per species (\bar{r} ; Tab. 1) as a representative emitting size.

Another possibility is that we are observing different molecular abundances at limited sensitivity. This means that we are able to detect the less abundant species only at the largest densities, hence closer to the protostar at small emitting radii. Among the various detected species, methanol (CH_3OH) is known to be the most abundant iCOM, and tracer of the protostellar environment at different scales (e.g. also outflows). Acetaldehyde (CH_3CHO), formamide (NH_2CHO), and glycolaldehyde (CH_2OHCHO), instead, seem to share similar lower abundances, and to trace the hot corino region only (see e.g. Taquet et al. 2015; López-Sepulcre et al. 2017; Belloche et al. 2020). While we cannot exclude a priori the aforesaid possibility, the fact that we observe a difference in the emitting size for all the iCOMs, also among the compact species, strongly suggests that the observed chemical segregation in IRAS 4A2 is real. On top of that, it should be noted that the observed difference in emitting sizes holds independently of the upper-state energy E_u , as we compared different iCOMs transitions at similar E_u precisely to account for gas excitation conditions.

A similar stratification has been observed in other two hot corinos, B335 (Okoda et al. 2022), between CH_3OH and NH_2CHO , and HH212, with CH_3OH , NH_2CHO , and CH_3CHO , (Lee et al. 2022), as well as toward some “hot cores” in high massive star forming regions (Jiménez-Serra et al. 2012; Calcutt et al. 2014; Gieser et al. 2019; Gieser et al. 2021). Bianchi et al. (2022) and Lee et al. (2022) associated this segregation to the different binding energy of the species. To prove this in IRAS 4A2, binding energies must be consistently derived for all the investigated iCOMs.

3.2. Gas temperature and column density estimates

In order to characterize the hot corino species column density and gas temperature, we analyzed the IRAS 4A2 spectrum performing a Gaussian fit on the emitting iCOMs lines (Fig A.1–A.6). Table A.1 reports the identified lines per species, with their spectral parameters and the results from the Gaussian fits. The line peak velocities lie between $+5.9$ and $+7.5$ km s^{-1} , consistent with the systemic velocity of IRAS 4A2 ($+6.8$ km s^{-1} ; Choi 2001) given the channel resolution of ~ 1.4 km s^{-1} . At this spectral resolution we do not detect significant deviations of the line profiles from a thermally broadened Gaussian. Note that we excluded from the analysis heavily blended transitions where we could not disentangle the emission.

The standard Rotational Diagram (RD) method (Blake et al. 1987; Turner 1991; Goldsmith & Langer 1999; Mangum & Shirley 2015) assumes local thermodynamic equilibrium (LTE) and optically-thin line emission. While LTE is generally valid due to the high densities of the probed region (higher than the

species critical density; De Simone et al. 2020a, 2022a), the optical depth assumption is likely not applicable for most of the iCOMs targeted here. This can lead to a potential underestimation of the upper-state populations of these transitions (Taquet et al. 2015; De Simone et al. 2020a).

Methanol (CH_3OH) is known to be very abundant and optically-thick in Class 0 sources, including IRAS 4A2. It is also one of the very few complex organic molecules for which collisional coefficients have been computed in order to perform a non-LTE analysis. We therefore performed a non-LTE analysis via our custom large velocity gradient (LVG) code `gre1vg` (Ceccarelli et al. 2003; De Simone et al. 2020a). With this, we fit the observed molecular line intensities and compared them with the predicted values using a chi-square minimization ($\tilde{\chi}^2$), accounting for line opacity. More details on the method are in App. C. Table 1 and Fig. 3 report the 1σ confidence level range for column density and temperature assuming a $0''.3$ emitting size, as derived from the CH_3OH integrated intensity maps. The resulting reduced chi-square is 0.6. With an LTE rotational diagram, at 1σ the resulting column density is constrained to $0.9\text{--}1.0$ 10^{18} cm^{-2} , and the temperature to $148\text{--}168$ K. In comparison, the LTE rotational diagram leads to a lower column density by a factor ~ 2 , while overestimating the temperature by a factor ~ 1.3 . The detected lines are too few to perform a statistically significant LTE population diagram analysis.

For the other iCOMs, lacking collisional coefficients for an LVG analysis, we used where possible the population diagram (PD) approach (Goldsmith & Langer 1999), which corrects rotational temperature and column density estimates for the self-consistently estimated line opacity. The methodology is described in detail in App. D. It is important to note that lines with high excitation ($E_u \geq 300$ K) may not be collisionally dominated, but rather radiatively pumped by the infrared field of the protostar (Tielens 2005). Therefore, they may not represent the actual kinetic temperature of the gas and may bias the population diagram results. Including radiative pumping would require detailed physical and chemical modeling of the envelope that is beyond the scope of this work. Because of this, to be on the safe side, at first we restricted the analysis to lines with $E_u \leq 300$ K (Tab. D.1 and Fig. D.1), with resulting reduced chi-square at 1σ of 0.6 (HCOOCH_3), 0.4 ($\text{CH}_3\text{CH}_2\text{OH}$), and 0.6 (CH_2OHCHO). Then, we repeated the analysis accounting for all detected lines, including the ones with $E_u > 300$ K (Fig. 4). We found that the best-fit results, column densities and temperatures, are consistent between the two cases. Considering all lines, we obtain 1σ confidence level ranges with $\tilde{\chi}^2$ values of 1.0 (HCOOCH_3), 0.9 ($\text{CH}_3\text{CH}_2\text{OH}$), and 0.5 (CH_2OHCHO). The best fits to the population diagram (see Fig. 4 and D.1) are similar in the two cases, implying that the bulk of the emission of the two groups of transitions (with E_u below and above 300 K) can be represented by the same physical conditions. In light of these results, we conclude that, in our case, the radiative pumping contribution may be negligible and we therefore rely on the results considering all transitions, which also allow more reliable 1σ estimates. Note that for glycolaldehyde (CH_2OHCHO) the FAUST data only cover transitions with high E_u . We therefore complemented our dataset with the sample from Taquet et al. (2015), as it covers transitions with E_u below 200 K, accounting for the different beam size ($\sim 2''$). We confirm that most of the lines are optically-thick ($\tau > 1$), justifying the requirement for the population diagram analysis. The acetaldehyde (CH_3CHO) transitions are too few to perform a statistically significant PD analysis. Thus, we relied on the RD analysis; the results are reported in Tab. 1 and Fig. E.1. Finally, the few detected formamide (NH_2CHO) lines

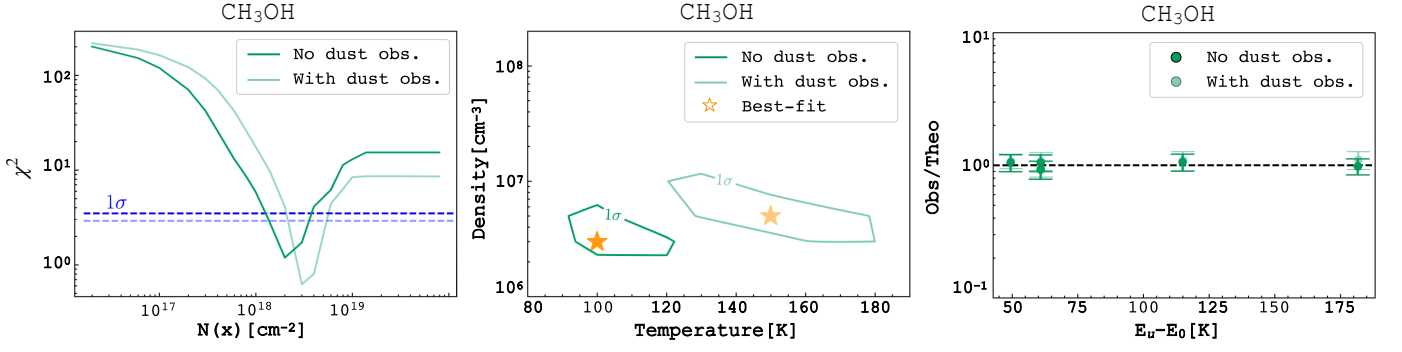


Fig. 3. Non-LTE LVG fitting results for methanol (CH₃OH) with (*full color*) and without (*shaded*) considering the contribution from mm foreground dust absorption (see Sec. 3.2). *Left*: χ^2 minimisation for the total column density $N_{\text{CH}_3\text{OH}}$ (A-type plus E-type). *Middle*: Density–temperature χ^2 contour plots showing 1 σ confidence level, assuming the best-fit value of $N_{\text{CH}_3\text{OH}} = 2 \times 10^{18}$ cm⁻² and a source size of 0".3. The best-fit solutions are marked by the star. *Right*: Observed line integrated intensities versus modeled ones as a function of the upper-state energy level value with respect to the lowest value.

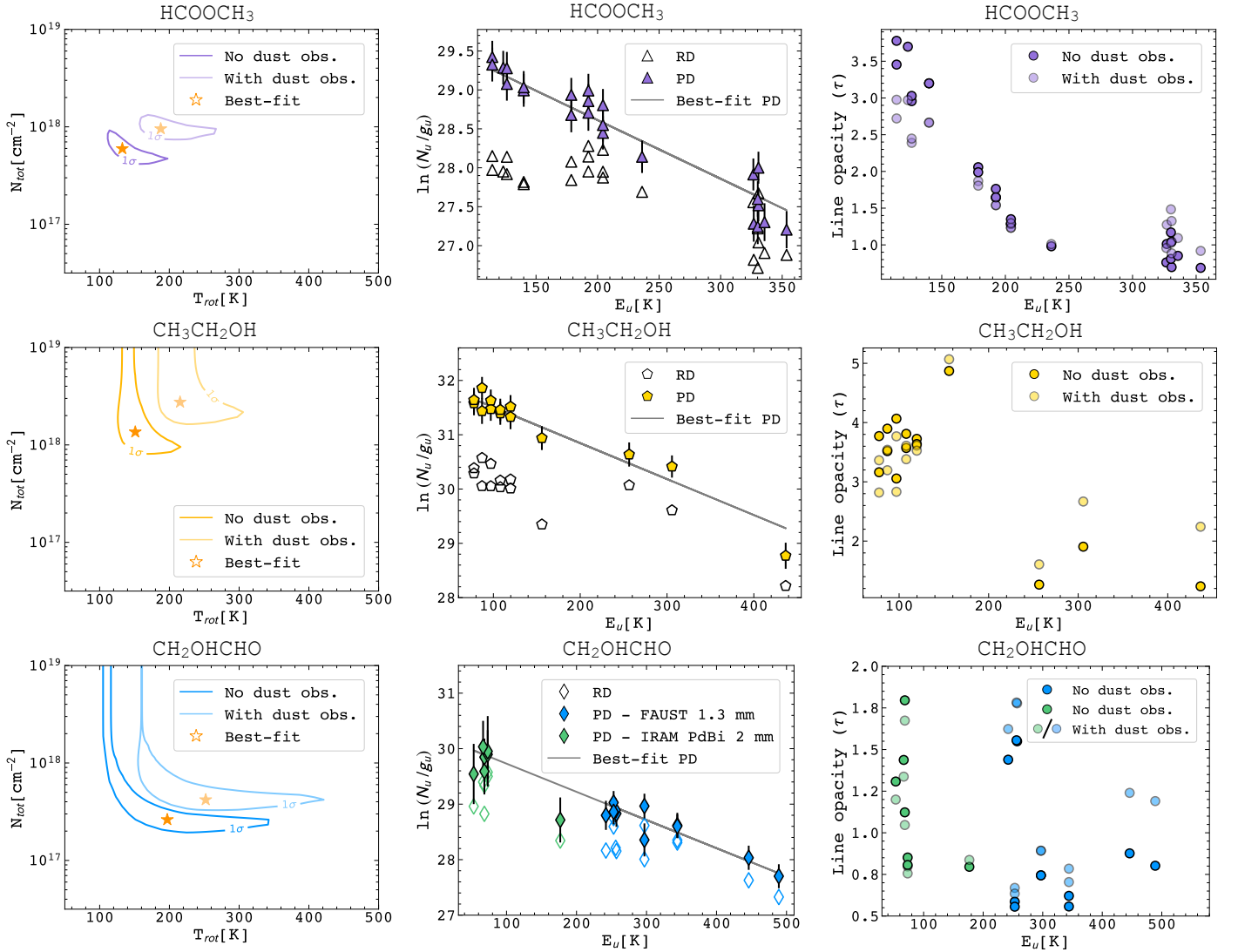


Fig. 4. LTE population diagrams (PD) of methyl formate (HCOOCH₃), ethanol (CH₃CH₂OH), and glycolaldehyde (CH₂OHCHO). For CH₂OHCHO, we complemented our dataset (*blue diamonds*) with the dataset of Taquet et al. (2015) (*green diamonds*). The results are plotted with (*shaded*) and without (*full color*) the mm dust obscuration factor. *Left*: Column density–temperature reduced χ^2 contour plots. The shaded and solid colored lines indicate the 1 σ confidence ranges. The star marks the best-fit value in the two cases. *Center*: Observed transitions corrected for the line opacity calculated at the best-fit values. The grey solid line refers to the best-fit of the data points (not corrected for dust obscuration). Empty markers indicate the points not corrected for line opacity, whose fit is the rotational diagram (RD). *Right*: Line opacity as a function of the upper-state energy of the best-fit values.

Table 1. 1σ confidence level results of the iCOMs molecular lines analysis and line emitting radius fit toward IRAS 4A2.

Species	Physical parameters				Image fitting	
	No dust obscuration		With dust obscuration		\bar{r}^a [au]	θ_{source}^b [arcsec]
T_{gas} [K]	N_{tot} [cm $^{-2}$]	T_{gas} [K]	N_{tot} [cm $^{-2}$]			
non-LTE LVG						
CH ₃ OH	90-120	$1.4\text{-}4 \times 10^{18}$	100-140	3×10^{18}	40.1 (0.8)	0.30
LTE population diagram (PD)						
HCOOCH ₃	110-200	$0.4\text{-}1.0 \times 10^{18}$	160-270	$0.8\text{-}1.3 \times 10^{18}$	36.0 (1.0)	0.26
CH ₃ CH ₂ OH	130-215	$>8 \times 10^{17}$	190-310	$>1.8 \times 10^{18}$	27.0 (0.8)	0.19
CH ₂ OHCHO	110-340	$>2 \times 10^{17}$	160-430	$>3.5 \times 10^{17}$	22.0 (1.0)	0.15
LTE rotational diagram (RD)						
CH ₃ CHO	180-228	$2.1\text{-}3.1 \times 10^{17}$	180-228	$3.3\text{-}4.7 \times 10^{17}$	28.0 (0.9)	0.20
NH ₂ CHO	197 ^c	$1.4\text{-}1.7 \times 10^{16}$	197 ^c	$2.1\text{-}2.5 \times 10^{16}$	23.0 (0.6)	0.16

^aWeighted average emitting radius. The uncertainties are reported in round parentheses. ^bSource size adopted for the analysis. ^cFixed as the best-fit temperature derived for CH₂OHCHO.

span a too small range of E_u to obtain reliable results from a rotational diagram. Nonetheless, given that NH₂CHO traces a similar spatial scale to CH₂OHCHO, we derived a lower limit on the column density (see Tab. 1), assuming the same best-fit temperature derived for CH₂OHCHO.

4. Discussion

4.1. The effect of millimeter foreground dust absorption

There are several possible mechanisms by which the observed molecular line emission may be obscured or otherwise reduced in the presence of optically-thick dust.

First, Class 0/I sources may be embedded in envelopes which often are optically-thick at mm/sub-mm wavelengths (Miotello et al. 2014; Galván-Madrid et al. 2018; Galametz et al. 2019). In this case, the foreground dust may absorb the molecular emission, what we call here *millimeter dust obscuration*. This leads to a non-detection of iCOMs at millimeter wavelengths (e.g. López-Sepulcre et al. 2017; De Simone et al. 2017; Belloche et al. 2020), or to the underestimation of the molecular column density inferred from optically-thin lines, or an underestimation of both column density and temperature when the optical depth of the lines is not negligible (De Simone et al. 2020a). Indeed, even if the dust is co-spatial with the gas, in the case of optically-thick dust and LTE molecules in emission, the line emission will be inseparable from the dust continuum emission. Therefore, the process of continuum subtraction will result in reduced (or apparently absent, or negative) line emission, regardless of the lines being intrinsically optically-thin or optically-thick.

As another possibility, if the molecular gas resides in front of optically-thick dust continuum emission, then after continuum subtraction the molecular lines may appear either in emission or absorption, or not appear at all, depending on the relative brightness temperatures of the line- and the dust-emitting regions. It can be difficult to distinguish between these scenarios without considering additional information about the source of the emission. Nevertheless, in all cases the derived molecular column densities and excitation temperatures can be significantly underestimated if the dust emission is not taken into account.

De Simone et al. (2020a, 2022b) uniquely estimated, using a combination of centimeter and millimeter observations, that the foreground dust may absorb about 30% at 143 GHz and 50% at 243 GHz the emission lines in IRAS 4A2 on scales of 0''26. Assuming all species on scales $< 0''26$ will be affected in some way by millimeter dust obscuration, we corrected the integrated line

flux for these factors (see the results in Tab. 1). In the PD and the LVG analysis, we found a systematic shift toward higher temperatures by 50–100 K and higher column densities by a factor of about 1.6 (2.2 for CH₃CH₂OH). For acetaldehyde (CH₃CHO) and formamide (NH₂CHO), we found a similar increase in column density from the RD analysis.

We compared our estimates to the literature (Taquet et al. 2015; De Simone et al. 2017, 2020a; López-Sepulcre et al. 2017; Belloche et al. 2020). In particular, Belloche et al. (2020) were the first to isolate IRAS 4A2 as a compact hot corino, yet, higher spatial resolution, achieved with this work, was necessary to spatially resolve the emitting size of various iCOMs. The values derived for methanol (CH₃OH) correcting for dust obscuration are consistent at 1σ ($\chi^2 = 0.3$) with those derived at centimeter wavelengths by De Simone et al. (2020a). The foreground dust absorption affects column density and temperature similarly to the line opacity (respectively with increasing factors of ~ 1.4 and ~ 3), with respect to the LTE rotational diagram method. For the other iCOMs, our new estimates generally point towards higher column densities and higher temperatures than previously measured. These discrepancies are due to a combination of line optical depth and foreground dust absorption effects.

Taking into account the foreground dust absorption and the measured line opacities, we do not observe systematic differences for linewidths and position angles among the different molecular species (see Tab. A.1). Only CH₃OH shows slightly larger linewidths, on average ~ 4 km s $^{-1}$ instead of ~ 3.5 km s $^{-1}$ as for the other species. This could be due to the fact that methanol's transitions may trace, particularly at low upper-state energy, other physical processes in the protostellar environment, such as outflowing material (e.g. De Simone et al. 2024). From the measured position angles, we estimate an inclination angle in the range of 11–56 degrees. However, the measured linewidths and position angles are uncertain, and the error bars, especially for the latter, are often large. A larger spectral resolution is required to conduct a detailed study of the kinematics of the IRAS 4A system.

4.2. The gas temperature profile of the IRAS 4A2 hot corino

The iCOMs spatial segregation together with the temperature estimate allow us to tentatively derive the gas temperature profile of IRAS 4A2 as a function of radial distance. Fig. 5 shows the derived gas temperatures (with and without accounting for the mm dust obscuration) versus the deconvolved emitting size

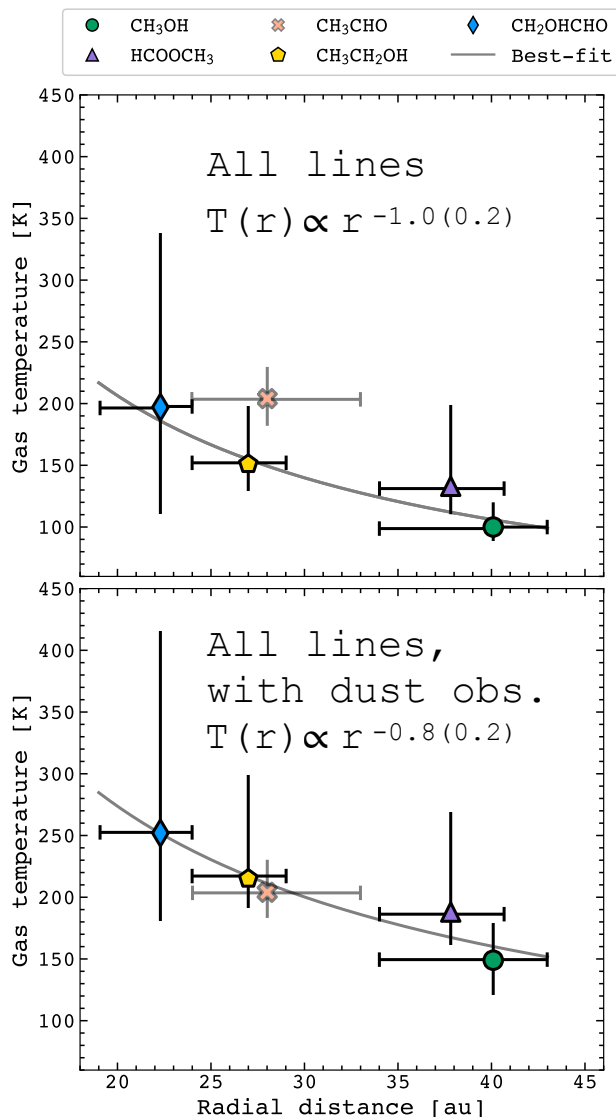


Fig. 5. T-r profile of IRAS 4A2. Gas temperatures are derived accounting for all transitions and for the mm dust obscuration (*bottom*). The colored data points mark the best-fit gas temperature derived for each species as a function of the average emitting radius \bar{r} . The emitting radius error bar encompasses the observed range of sizes per species. The error bar on the temperature is the 1σ confidence range of the LTE rotational diagram analysis (CH₃CHO), LTE population diagram analysis (HCOOCH₃, CH₃CH₂OH, and CH₂OHCHO), and of the non-LTE LVG analysis for CH₃OH. The grey solid line in both panels is the best fit to the data points excluding CH₃CHO (see Sec. 3.2).

derived for each species, as a probe of the distance from the protostellar center. For completeness, Fig. E.2 shows the resulting temperature profile accounting only for iCOMs transitions with $E_u \leq 300$ K. We naturally excluded from the fit formamide (NH₂CHO), for which it was not possible to reliably estimate the rotational temperature, and acetaldehyde (CH₃CHO), for which we could not estimate self-consistently the contribution of the line opacity. Nevertheless, we included as a reference the CH₃CHO temperature derived with the RD in Fig. 5.

From theory, the dust temperature is expected to radially behave like a power law: $T(r) \propto r^q$ (Beckwith et al. 1990; Motte & André 2001; Andrews & Williams 2007). At large densities, such as in hot corinos, gas and dust are likely thermally coupled (Ceccarelli et al. 1996; Maret et al. 2002; Crimier et al. 2009;

Crimier et al. 2010). By fitting the data points with a power-law function, we find an exponent $q = -1.0 \pm 0.2$. Accounting for the millimeter dust obscuration, we obtain a consistent result of $q = -0.8 \pm 0.2$. A similar attempt in low mass protostars has been performed at larger scales, focusing on modeling and/or observing simpler molecular species (e.g., CO, H₂CO, H₂CS) and hinting to a profile of spherically collapsing envelopes (Ceccarelli et al. 2000; Maret et al. 2002; Crimier et al. 2010), or rotationally supported disk (Jacobsen et al. 2018; van 't Hoff et al. 2020). Our fit implies a power-law steeper than what expected in an optically-thin spherical collapsing envelope ($q \sim 0.4-0.5$; Ceccarelli et al. 2000; Schöier et al. 2002; Crimier et al. 2010). Alternatively, we might be observing layers in the envelope where the dust optical depth is ≤ 1 (Adams & Shu 1986; Ceccarelli et al. 1996). Indeed, from the comparison with observations at centimeter wavelength, De Simone et al. (2020a) estimated a dust foreground absorption of 30% circa, which corresponds to a dust optical depth of about 0.3. This is reasonable since a completely optically-thick envelope ($\tau > 1$) would have completely absorbed the molecular line emission, as in the case of the IRAS 4A1 binary component (De Simone et al. 2020a). Another possibility is that, to explain the high gas temperature observed at these compact scales, the iCOMs are probing a disk-like structure that is gravitationally unstable Zamponi et al. (2021).

To disentangle which contribution dominates, we need a detailed thermochemical model to reproduce the T-r profile, and high angular (about 5–10 au) observations at higher spectral resolution so as to resolve the kinematics of the most compact iCOMs species.

5. Conclusions

Within the FAUST framework we observed for the first time a chemical segregation of six iCOMs in the IRAS 4A2 hot corino.

1. The detected iCOMs show different emitting sizes of increasing outer radius, with methanol (CH₃OH) being the most extended, at ~ 40 au, glycolaldehyde (CH₂OHCHO) and formamide (NH₂CHO) the most compact and partially unresolved, at $\sim 22-23$ au, and methyl formate (HCOOCH₃), acetaldehyde (CH₃CHO) and ethanol (CH₃CH₂OH) in between, with an outer radius located at $\sim 28-36$ au.
2. Using a multi-line analysis, both in LTE and non-LTE (the latter for CH₃OH only), we derived gas temperatures and molecular column densities corrected for (i) line opacity and for (ii) the foreground dust absorption at millimeter wavelengths. The latter implies higher gas temperatures by 50–100 K, and higher column densities by a factor ~ 1.6 .
3. We retrieved a gas temperature profile (T-r) at scales of 20–50 au (in radius) directly from the observed molecular line emission. The higher gas temperature (up to 200–250 K) is associated with the more compact iCOM emission. The power-law T-r exponent q is about $-0.8/-1.0$, inconsistent with an optically-thin spherical collapsing envelope. This may hint at a partially optically-thick protostellar envelope, or a gravitationally unstable disk-like structure in IRAS 4A2.

At millimeter wavelengths, the optical thickness of foreground dust and the molecular line opacity are crucial parameters to determine unbiased gas temperatures and molecular abundances. This work highlights how the mm dust opacity affects not only the estimates of the column densities and/or abundances of the observed molecular species, but also the temperature of the traced gas. This is particularly evident for the more abundant

species, e.g. methanol (CH₃OH), which has optically thick emission lines. However, high spatial and spectral resolution observations, paired with a large bandwidth, are still needed to spatially resolve the molecular emission as well as the gas kinematics, especially of the most compact iCOM species. This will also allow to clarify the exact source geometry.

This work opens the way to many future perspectives. First of all, there is a need to derive similar temperature profiles for other Class 0/I protostars, and compare them with the predictions on embedded young disks from the latest simulations (e.g. Lebreuilly et al. 2023). Also, as mentioned in Sect. 3.1, there is a need to link the stratified chemical structure to the iCOMs binding energies, and perform a similar study on other hot corino sources, which also implies follow-ups at higher angular resolution. Such work also sets the ground for the upcoming centimeter facilities (e.g., SKA⁵ and ngVLA⁶), as well as the new ALMA wide band sensitivity upgrade (Ossenkopf-Okada et al. 2023). Centimeter observations are particularly crucial to fully characterize hot corinos both from a chemical and physical perspective. With SKA and ngVLA, we will access much larger and complex iCOMs species than methanol, in a wavelength regime where the dust is more likely optically-thin, and spectral line blending and line confusion are reduced. At the same time, ALMA WSU will provide us with a large bandwidth to detect more transitions per species and therefore perform a more robust multi-line analysis.

Acknowledgements. We thank the anonymous referee for all the useful comments and suggestions that greatly improved the manuscript. This Paper makes use of the following ALMA data: ADS/JAO.ALMA#2018.1.01205.L (PI: S. Yamamoto). ALMA is a partnership of the ESO (representing its member states), the NSF (USA) and NINS (Japan), together with the NRC (Canada) and the NSC and ASIAA (Taiwan), in cooperation with the Republic of Chile. The Joint ALMA Observatory is operated by the ESO, the AUI/NRAO, and the NAOJ. This work was partly supported by the Italian Ministero dell Istruzione, Università e Ricerca through the grant Progetti Premiali 2012 – iALMA (CUP C52I13000140001). This project has received funding from the European Union’s Horizon 2020 research and innovation programme under the Marie Skłodowska-Curie grant agreement No 823823 (DUSTBUSTERS) and from the European Research Council (ERC) via the ERC Synergy Grant *ECOGAL* (grant 855130). Part of the analysis and work that led to this study were carried out during the May 2023 workshop at the Institut Pascal in Saclay, which was funded and organized as part of the *ECOGAL* collaboration. JF acknowledges financial support from the DIFA and the ESO Office for Science. CICO, LP, GS and EB acknowledge the PRIN-MUR 2020 BEYOND-2p (Astrochemistry beyond the Second period elements, Prot. 2020AFB3FX), the project ASI-Astrobiologia 2023 MIGLIORA (Modeling Chemical Complexity, F83C23000800005), the INAF-GO 2023 fundings PROTO-SKA (Exploiting ALMA data to study planet forming disks: preparing the advent of SKA, C13C23000770005), the INAF Mini-Grant 2022 “Chemical Origins” (PI: L. Podio), the INAF Mini-grant 2023 TRIESTE (“TRacing the chemical hEritage of our originS: from proTostars to planEts”; PI: G. Sabatini), and the National Recovery and Resilience Plan (NRRP), Mission 4, Component 2, Investment 1.1, Call for tender No. 104 published on 2.2.2022 by the Italian Ministry of University and Research (MUR), funded by the European Union – NextGenerationEU – Project Title 2022JC2Y93 Chemical Origins: linking the fossil composition of the Solar System with the chemistry of protoplanetary disks – CUP J53D23001600006 - Grant Assignment Decree No. 962 adopted on 30.06.2023 by the Italian Ministry of Ministry of University and Research (MUR). E.B. also acknowledges the contribution of the Next Generation EU funds within the National Recovery and Resilience Plan (PNRR), Mission 4 - Education and Research, Component 2 - From Research to Business (M4C2), Investment Line 3.1 - Strengthening and creation of Research Infrastructures, Project IR0000034 – “STILES - Strengthening the Italian Leadership in ELT and SKA”. I.J.-S acknowledges funding from grant PID2022-136814NB-I00 funded by MICIU/AEI/ 10.13039/501100011033 and by “ERDF/EU”. SBC was supported by the NASA Planetary Science Division Internal Scientist Funding Program through the Fundamental Laboratory Research work package (FLaRe). M.B. acknowledges the support from the European Research Council (ERC) Advanced Grant MOPPEX 833460.

References

- Adams, F. C. & Shu, F. H. 1986, *ApJ*, 308, 836
 André, P. 2002, *EAS Publications Series*, 3, 1
 André, P., Ward-Thompson, D., & Barsony, M. 2000, in *Protostars and Planets IV*, ed. V. Mannings, A. P. Boss, & S. S. Russell, 59
 Andrews, S. M. & Williams, J. P. 2007, *The Astrophysical Journal*, 659, 705
 Beckwith, S. V. W., Sargent, A. I., Chini, R. S., & Guesten, R. 1990, *The Astrophysical Journal*, 99, 924
 Belloche, A., Maury, A. J., Maret, S., et al. 2020, *A&A*, 635, A198
 Bernabò, L. M., Turrini, D., Testi, L., Marzari, F., & Polychroni, D. 2022, *ApJ*, 927, L22
 Bianchi, E., López-Sepulcre, A., Ceccarelli, C., et al. 2022, *ApJ*, 928, L3
 Blake, G. A., Sutton, E. C., Masson, C. R., & Phillips, T. G. 1987, *The Astrophysical Journal*, 315, 621
 Bottinelli, S., Ceccarelli, C., Lefloch, B., et al. 2004, *The Astrophysical Journal*, 615, 354
 Calcutt, H., Viti, S., Codella, C., et al. 2014, *MNRAS*, 443, 3157
 Caselli, P. & Ceccarelli, C. 2012, *A&ARv*, 20, 56
 Ceccarelli, C. 2004, in *Astronomical Society of the Pacific Conference Series*, Vol. 323, *Star Formation in the Interstellar Medium: In Honor of David Hollenbach*, ed. D. Johnstone, F. C. Adams, D. N. C. Lin, D. A. Neufeld, & E. C. Ostriker, 195
 Ceccarelli, C. 2023, in *European Conference on Laboratory Astrophysics ECLA2020. The Interplay of Dust*, 3–16
 Ceccarelli, C., Caselli, P., Fontani, F., et al. 2017, *The Astrophysical Journal*, 850, 176
 Ceccarelli, C., Castets, A., Caux, E., et al. 2000, *A&A*, 355, 1129
 Ceccarelli, C., Codella, C., Balucani, N., et al. 2023, in *Astronomical Society of the Pacific Conference Series*, Vol. 534, *Protostars and Planets VII*, ed. S. Inutsuka, Y. Aikawa, T. Muto, K. Tomida, & M. Tamura, 379
 Ceccarelli, C., Hollenbach, D. J., & Tielens, A. G. G. M. 1996, *The Astrophysical Journal*, 471, 400
 Ceccarelli, C., Maret, S., Tielens, A. G. G. M., Castets, A., & Caux, E. 2003, *A&A*, 410, 587
 Chahine, L., Ceccarelli, C., De Simone, M., et al. 2024, *MNRAS*, 531, 2653
 Choi, M. 2001, *The Astrophysical Journal*, 553, 219
 Codella, C., Ceccarelli, C., Chandler, C., et al. 2021, *Front. astron. space sci.*, 8, 227
 Collier, B., Krueger, K., Miller, I., et al. 2021, *ApJS*, 253, 40
 Costain, C. C. & Dowling, J. M. 1960, *J. Chem. Phys.*, 32, 158
 Crimier, Ceccarelli, C., Alonso-Albi, T., et al. 2010, *A&A*, 516, A102
 Crimier, N., Ceccarelli, C., Lefloch, B., & Faure, A. 2009, *A&A*, 506, 1229–1241
 De Simone, M., Ceccarelli, C., Codella, C., et al. 2020a, *ApJ*, 896, L3
 De Simone, M., Ceccarelli, C., Codella, C., et al. 2022a, *ApJ*, 935, L14
 De Simone, M., Codella, C., Ceccarelli, C., et al. 2022b, *Monthly Notices of the Royal Astronomical Society*, 512, 5214
 De Simone, M., Codella, C., Ceccarelli, C., et al. 2020b, *A&A*, 640, A75
 De Simone, M., Codella, C., Testi, L., et al. 2017, *A&A*, 599, A121
 De Simone, M., Podio, L., Chahine, L., et al. 2024, *A&A*, 686, L13
 Drouin, B. J. 2017, *Journal of Molecular Spectroscopy*, 340, 1
 Dubernet, M. L., Alexander, M. H., Ba, Y. A., et al. 2013, *A&A*, 553, A50
 Endres, C. P., Schlemmer, S., Schilke, P., Stutzki, J., & Müller, H. S. 2016, *Journal of Molecular Spectroscopy*, 327, 95, new Visions of Spectroscopic Databases, Volume II
 Galametz, M., Maury, A. J., Valdivia, V., et al. 2019, *A&A*, 632, A5
 Galván-Madrid, R., Liu, H. B., Izquierdo, A. F., et al. 2018, *ApJ*, 868, 39
 Gieser, C., Beuther, H., Semenov, D., et al. 2021, *A&A*, 648, A66
 Gieser, C., Semenov, D., Beuther, H., et al. 2019, *A&A*, 631, A142
 Goldsmith, P. F. & Langer, W. D. 1999, *ApJ*, 517, 209
 Herbst, E. & van Dishoeck, E. F. 2009, *Annual Reviews of Astronomy and Astrophysics*, 47, 427
 Ilyushin, V., Kryvda, A., & Alekseev, E. 2009, *Journal of Molecular Spectroscopy*, 255, 32
 Jacobsen, Jørgensen, J. K., van der Wiel, M. H. D., et al. 2018, *A&A*, 612, A72
 Jiménez-Serra, I., Zhang, Q., Viti, S., Martín-Pintado, J., & de Wit, W.-J. 2012, *The Astrophysical Journal*, 753, 34
 Johansen, A., Blum, J., Tanaka, H., et al. 2014, in *Protostars and Planets VI*, ed. H. Beuther, R. S. Klessen, C. P. Dullemond, & T. Henning, 547–570
 Johnson, D. R., Lovas, F. J., & Kirchhoff, W. H. 2009, *Journal of Physical and Chemical Reference Data*, 1, 1011
 Johnson, T. J., Sams, R. L., Profeta, L. T. M., et al. 2013, *Journal of Physical Chemistry A*, 117, 4096
 Karska, Herczeg, G. J., van Dishoeck, E. F., et al. 2013, *A&A*, 552, A141
 Kirchhoff, W. H. & Johnson, D. R. 1973, *Journal of Molecular Spectroscopy*, 45, 159
 Kleiner, I., Lovas, F. J., & Godefroid, M. 1996, *Journal of Physical and Chemical Reference Data*, 25, 1113
 Kristensen, van Dishoeck, E. F., Bergin, E. A., et al. 2012, *A&A*, 542, A8
 Kukolich, S. & Nelson, A. 1971, *Chemical Physics Letters*, 11, 383

⁵ <https://www.skao.int/en>

⁶ <https://ngvla.nrao.edu>

- Kurland, R. J. & Wilson, E. Bright, J. 2004, *The Journal of Chemical Physics*, 27, 585
- Lada, C. J. 1987, in *Star Forming Regions*, ed. M. Peimbert & J. Jugaku, Vol. 115, 1
- Lebreuilly, U., Hennebelle, P., Colman, T., et al. 2021, *ApJ*, 917, L10
- Lebreuilly, U., Hennebelle, P., Colman, T., et al. 2023, arXiv e-prints, arXiv:2310.19672
- Lebreuilly, U., Hennebelle, P., Colman, T., et al. 2024, *A&A*, 682, A30
- Lee, C.-F., Codella, C., Ceccarelli, C., & López-Sepulcre, A. 2022, *ApJ*, 937, 10
- López-Sepulcre, Sakai, N., Neri, R., et al. 2017, *A&A*, 606, A121
- Manara, C. F., Morbidelli, A., & Guillot, T. 2018, *A&A*, 618, L3
- Mangum, J. G. & Shirley, Y. L. 2015, *Publications of the Astronomical Society of the Pacific*, 127, 266
- Maret, S., Ceccarelli, C., Caux, E., Tielens, A. G. G. M., & Castets, A. 2002, *A&A*, 395, 573
- Maureira, M. J., Gong, M., Pineda, J. E., et al. 2022, *ApJ*, 941, L23
- Mauray, A. J., Belloche, A., André, P., et al. 2014, *A&A*, 563, L2
- Miotello, A., Testi, L., Lodato, G., et al. 2014, *A&A*, 567, A32
- Motte & André. 2001, *A&A*, 365, 440
- Müller, H. S. P., Schlöder, F., Stutzki, J., & Winnewisser, G. 2005, *Journal of Molecular Structure*, 742, 215
- Öberg, K. I. & Bergin, E. A. 2021, *Phys. Rep.*, 893, 1
- Okoda, Y., Oya, Y., Imai, M., et al. 2022, *ApJ*, 935, 136
- Ortiz-León, G. N., Loinard, L., Dzib, S. A., et al. 2018, *ApJ*, 869, L33
- Ossenkopf-Okada, V., Schaaf, R., Breloy, I., & Stutzki, J. 2023, *Physics and chemistry of star formation : the dynamical ISM across time and spatial scales : proceedings of the 7th Chile-Cologne-Bonn-Symposium*
- Pearson, J. C., Brauer, C. S., & Drouin, B. J. 2008, *Journal of Molecular Spectroscopy*, 251, 394, special issue dedicated to the pioneering work of Drs. Edward A. Cohen and Herbert M. Pickett on spectroscopy relevant to the Earth's atmosphere and astrophysics
- Pickett, H., POYNTER, R., COHEN, E., et al. 1998, *Journal of Quantitative Spectroscopy and Radiative Transfer*, 60, 883
- Rabli, D. & Flower, D. R. 2010, *MNRAS*, 406, 95
- Schöier, F. L., Jørgensen, J. K., van Dishoeck, E. F., & Blake, G. A. 2002, *A&A*, 390, 1001
- Sheehan, P. D. & Eisner, J. A. 2018, *ApJ*, 857, 18
- Taquet, V., López-Sepulcre, A., Ceccarelli, C., et al. 2015, *The Astrophysical Journal*, 804, 81
- Tielens, A. G. G. M. 2005, *The Physics and Chemistry of the Interstellar Medium*
- Tung, N.-D., Testi, L., Lebreuilly, U., et al. 2024, *The accuracy of ALMA estimates of young disk radii and masses. Predicted observations from numerical simulations*
- Turner, B. E. 1991, *The Astrophysical Journal, Supplement*, 76, 617
- Tychoniec, L., Manara, Carlo F., Rosotti, Giovanni P., et al. 2020, *A&A*, 640, A19
- van 't Hoff, M. L. R., van Dishoeck, Ewine F., Jørgensen, Jes K., & Calcutt, Hannah. 2020, *A&A*, 633, A7
- Xu, L.-H., Fisher, J., Lees, R., et al. 2008, *Journal of Molecular Spectroscopy*, 251
- Zamponi, J., Maureira, M. J., Zhao, B., et al. 2021, *Monthly Notices of the Royal Astronomical Society*, 508, 2583–2599
- Zucker, C., Schlafly, E. F., Speagle, J. S., et al. 2018, *ApJ*, 869, 83

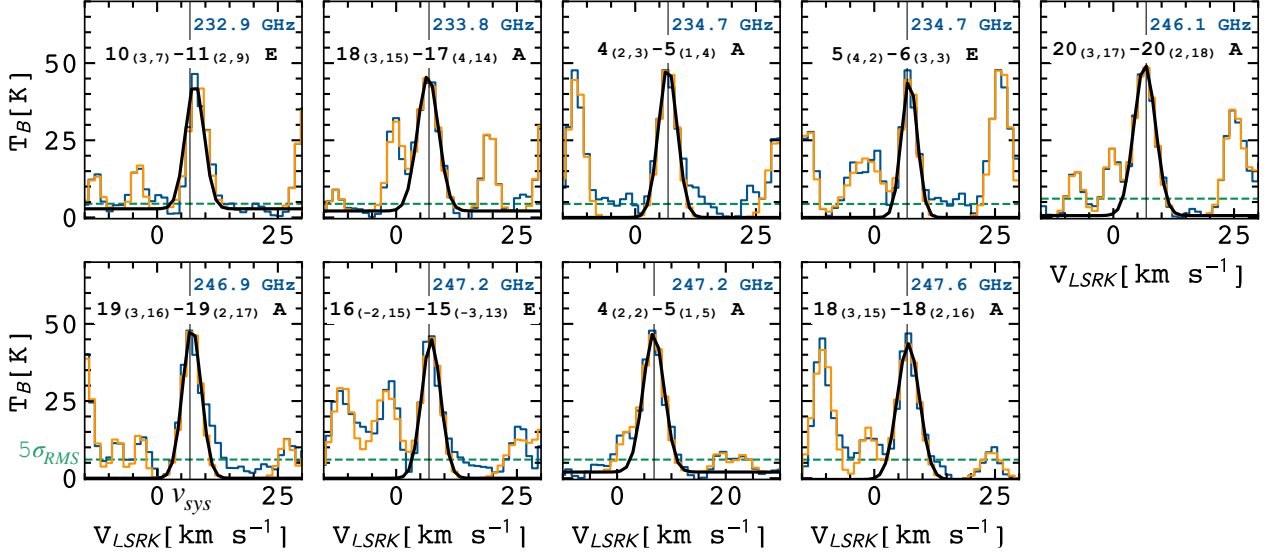
Appendix A: Detected lines, spectral parameters and fit results


Fig. A.1. Observed CH₃OH line spectra (in T_B scale) extracted at the continuum peak position of IRAS 4A2. The blue solid line indicates the baseline-subtracted spectrum, the orange line the best-fit model, and the black line the Gaussian profile of the labeled transition. The green dotted line marks the 5σ line cube RMS. The vertical black solid line indicates the system cloud LSR velocity ($+6.8$ km s⁻¹). The limits on the x-axis are occasionally redefined for visualization purposes.

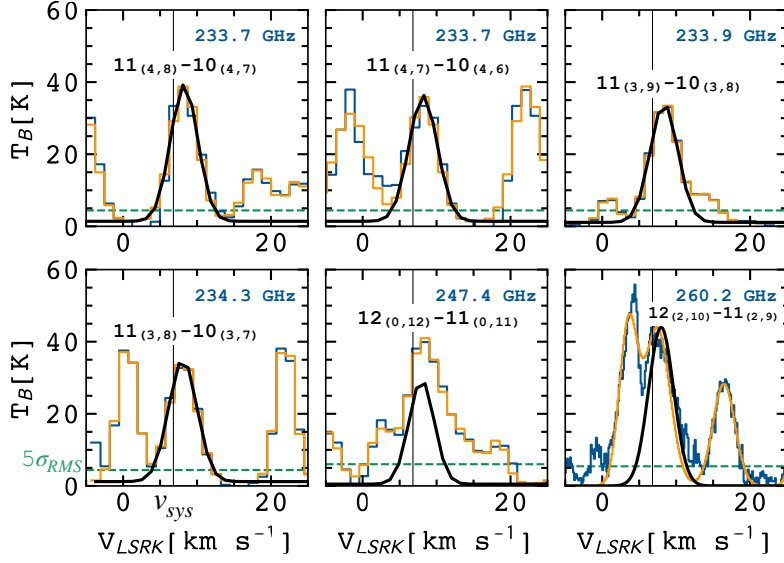


Fig. A.2. Same as Fig. A.1 for NH₂CHO.

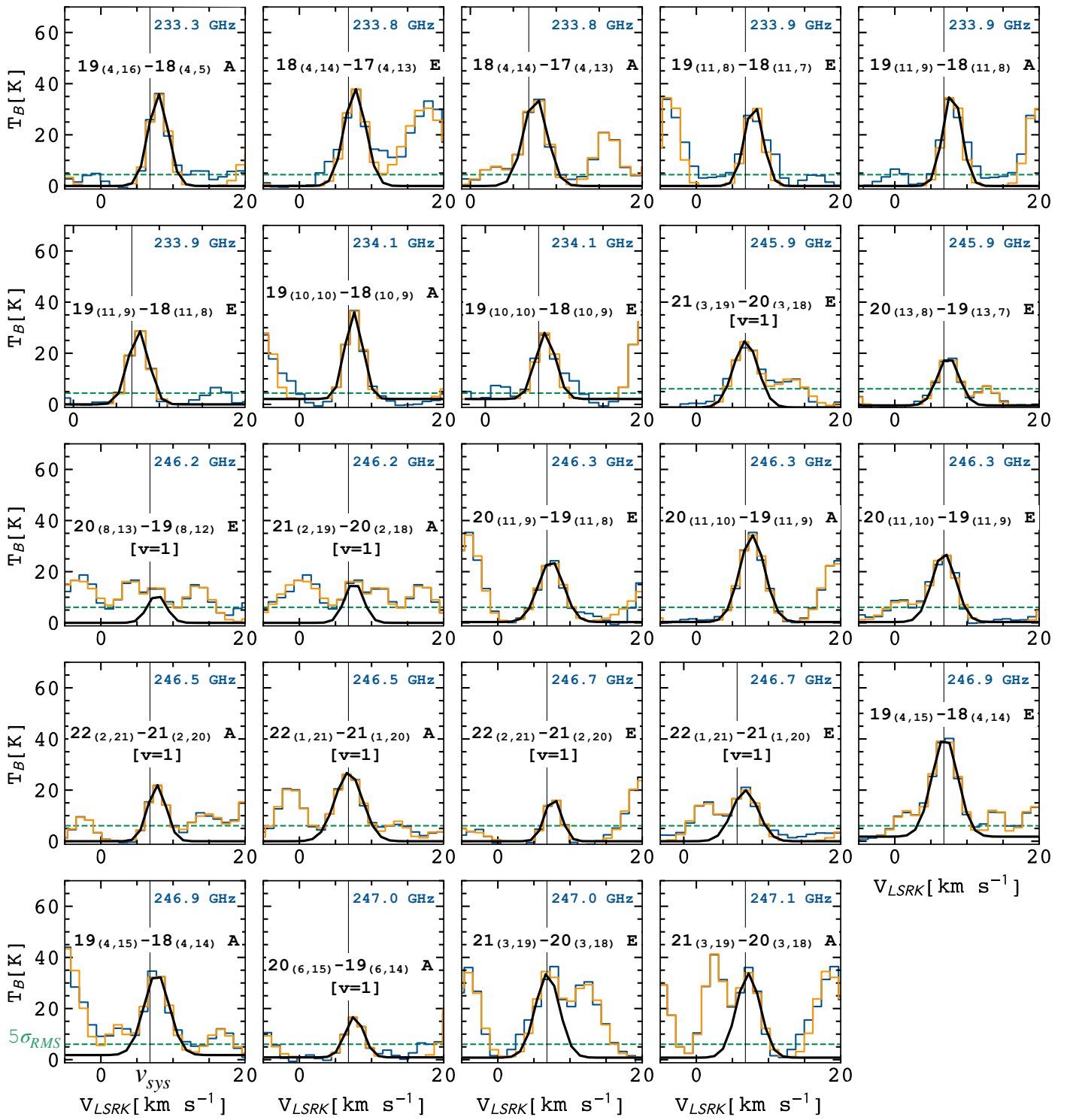


Fig. A.3. Same as Fig. A.1 for HCOOCH₃. The limits on the x-axis are occasionally redefined for visualization purposes.

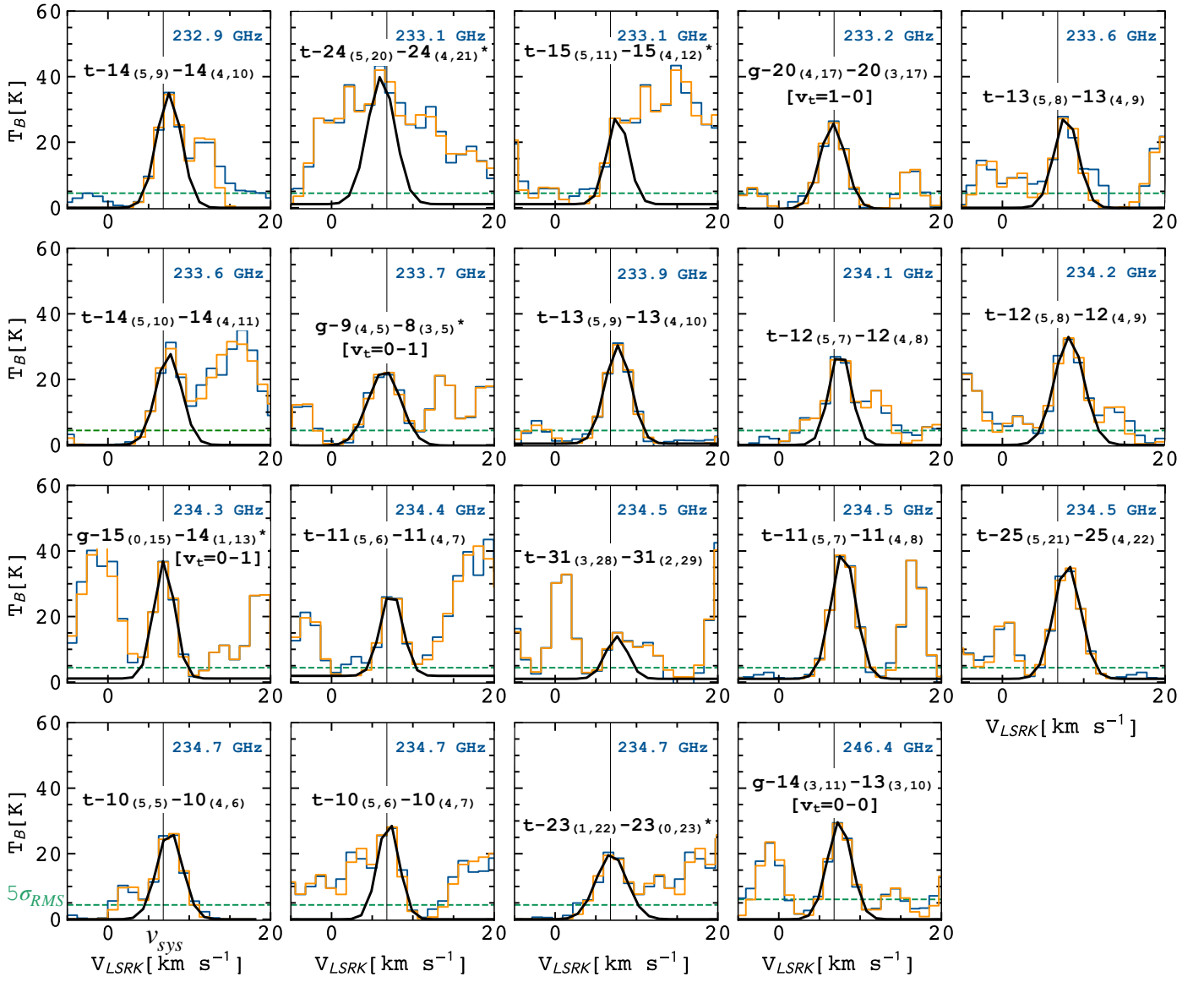


Fig. A.4. Same as Fig. A.1 for $\text{CH}_3\text{CH}_2\text{OH}$. Transitions with an asterisk have been excluded from the analysis due to contamination from other species.

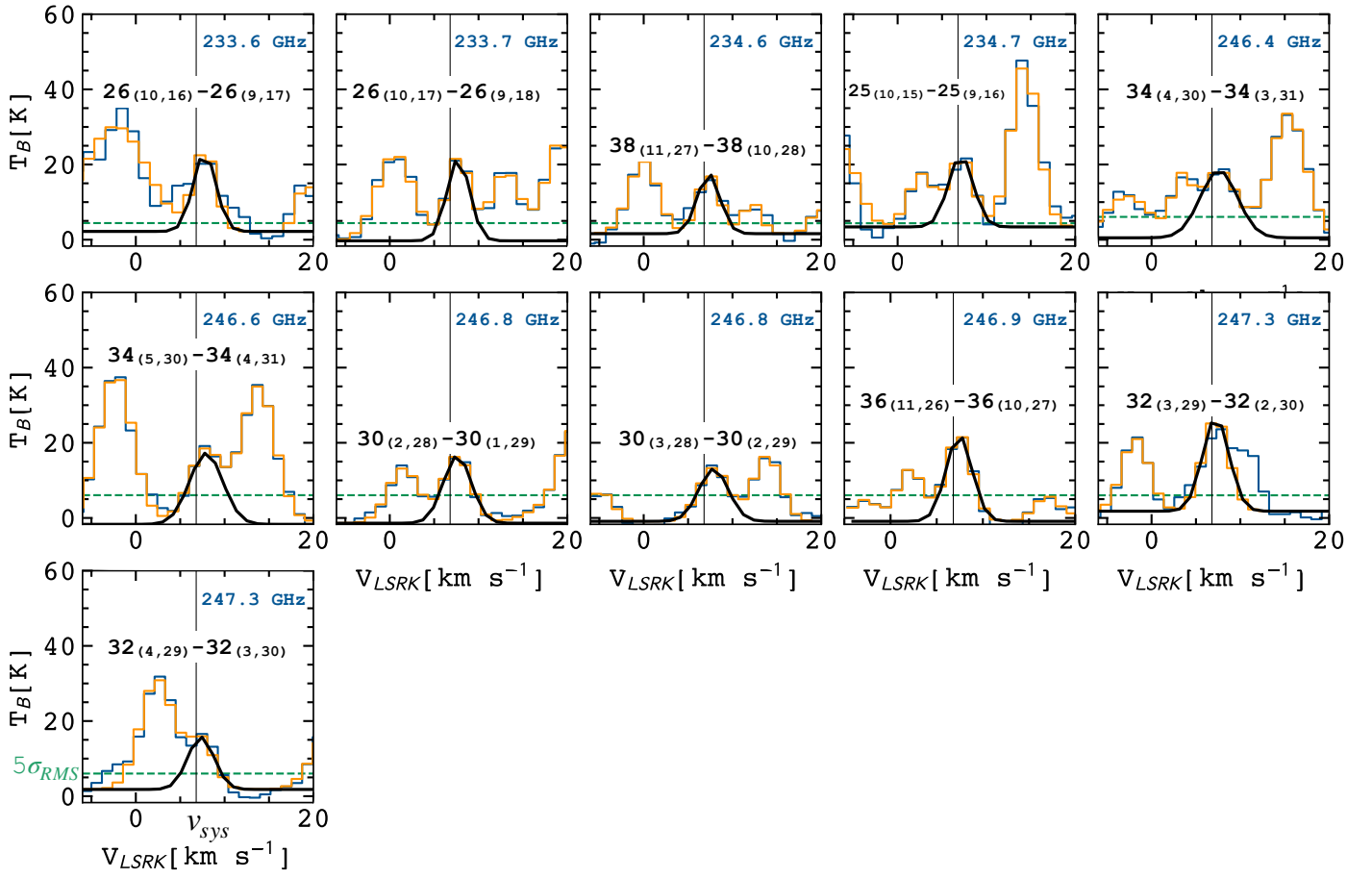


Fig. A.5. Same as Fig. A.1 for CH_2OHCHO . The limits on the x-axis are occasionally redefined for visualization purposes.

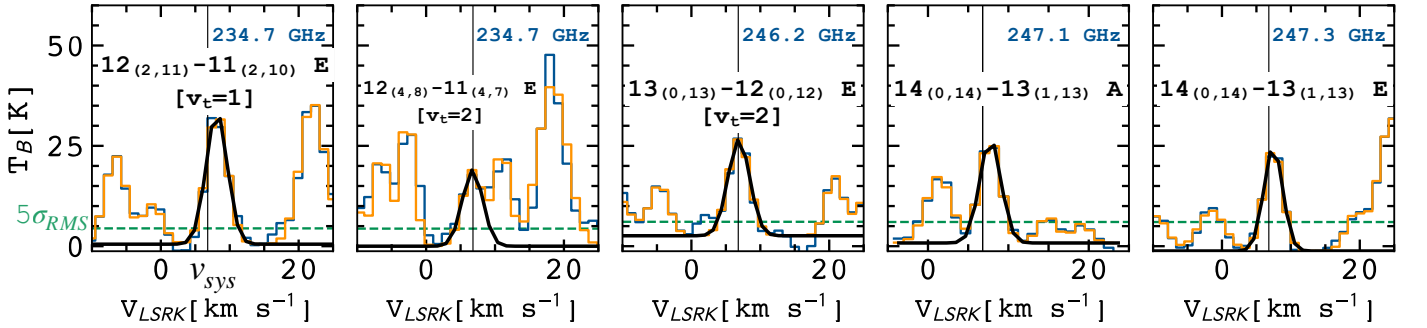


Fig. A.6. Same as Fig. A.1 for CH_3CHO . The limits on the x-axis are occasionally redefined for visualization purposes.

Table A.1. Spectral properties and Gaussian fit parameters of iCOMs lines detected towards the IRAS 4A2 continuum peak extracted spectrum.

Transition ^a	Spectroscopic parameters				Gaussian fit results		
	ν^a [MHz]	E_u^a [K]	$\text{Log}_{10} (A_{ul}/s^{-1})^a$	g_u^a	$\int T_B d\nu^b$ [K km s ⁻¹]	V_{peak}^b [km s ⁻¹]	FWHM^b [km s ⁻¹]
CH₃OH							
10 _(3,7) – 11 _(2,9) E	232945.797	191	-4.7	84	196 (10)	7.19 (0.10)	4.5 (0.3)
18 _(3,15) – 17 _(4,14) A	233795.666	447	-4.7	148	237 (11)	5.99 (0.10)	5.1 (0.3)
4 _(2,3) – 5 _(1,4) A	234683.370	61	-4.7	36	237 (11)	6.16 (0.13)	4.5 (-)
5 _(4,2) – 6 _(3,3) E	234698.519	123	-5.2	44	183 (15)	6.67 (0.14)	3.8 (0.3)
20 _(3,17) -20 _(2,18) A	246074.605	537	-4.1	164	267 (11)	5.91 (0.08)	5.2 (0.2)
19 _(3,16) – 19 _(2,17) A	246873.301	491	-4.1	156	236 (11)	6.61 (0.13)	4.5 (-)
16 _(-2,15) – 15 _(-3,13) E	247161.950	338	-4.6	132	224 (19)	6.65 (0.19)	4.6 (0.5)
4 _(2,2) – 5 _(1,5) A	247228.587	61	-4.7	36	217 (8)	6.12 (0.07)	4.55 (0.19)
18 _(3,15) – 18 _(2,16) A	247610.918	447	-4.1	148	250 (15)	6.46 (0.13)	5.4 (0.3)
HCOOCH₃							
19 _(4,16) -18 _(4,15) A	233226.788	123	-3.7	78	121 (10)	7.34 (0.13)	3.2 (0.3)
18 _(4,14) -17 _(4,13) E	233753.960	114	-3.8	74	141 (8)	7.10 (0.12)	3.5 (-)
18 _(4,14) -17 _(4,13) A	233777.521	114	-3.8	74	118 (10)	6.97 (0.13)	3.2 (0.3)
19 _(11,8) -18 _(11,7) E	233845.233	193	-3.9	78	103 (9)	7.36 (0.15)	3.0 (-)
19 _(11,9) -18 _(11,8) A	233854.286	193	-3.9	78	118 (9)	7.36 (0.13)	3.0 (-)
19 _(11,9) -18 _(11,8) E	233867.193	193	-3.9	78	85 (10)	6.98 (0.16)	2.8 (0.4)
19 _(10,10) -18 _(10,9) A	234124.883	179	3.9	78	105 (9)	6.95 (0.11)	2.9 (0.3)
19 _(10,10) -18 _(10,9) E	234134.600	179	-3.9	78	83 (8)	7.07 (0.15)	3.0 (-)
21 _(3,19) -20 _(3,18) E [v=1]	245846.914	327	-3.7	86	57 (18)	6.24 (0.16)	4.0 (-)
20 _(13,8) -19 _(13,7) E	245903.680	236	-3.9	82	71 (4)	6.80 (0.07)	3.5 (0.19)
20 _(8,13) -19 _(8,12) E [v=1]	246184.177	354	-3.7	82	46 (6)	7.14 (-)	3.0 (-)
21 _(2,19) -20 _(2,18) A [v=1]	246187.016	327	-3.7	86	52 (6)	6.97 (-)	3.0 (-)
20 _(11,9) -19 _(11,8) E	246285.400	204	-3.8	82	103 (8)	6.75 (0.13)	4.1 (0.3)
20 _(11,10) -19 _(11,9) A	246295.135	204	-3.8	82	147 (8)	7.13 (0.08)	4.1 (0.2)
20 _(11,10) -19 _(11,9) E	246308.272	204	-3.8	82	112 (8)	6.20 (0.12)	3.9 (0.3)
22 _(2,21) -21 _(2,20) A [v=1]	246461.167	331	-3.7	90	69 (4)	7.17 (0.11)	3.0 (0.3)
22 _(1,21) -21 _(1,20) A [v=1]	246488.433	331	-3.7	90	130 (6)	6.24 (0.09)	4.5 (0.2)
22 _(2,21) -21 _(2,20) E [v=1]	246706.504	330	-3.7	90	50 (5)	7.06 (0.13)	2.7 (0.3)
22 _(1,21) -21 _(1,20) E [v=1]	246731.729	330	-3.7	90	83 (9)	7.23 (0.19)	3.9 (0.5)
19 _(4,15) -18 _(4,14) E	246891.611	126	-3.7	78	176 (11)	6.35 (0.10)	4.2 (0.3)
19 _(4,15) -18 _(4,14) A	246914.658	126	-3.7	78	141 (11)	7.12 (0.12)	4.1 (0.3)
20 _(6,15) -19 _(6,14) A [v=1]	246985.225	336	-3.7	82	51 (7)	7.04 (0.17)	3.0 (0.4)
21 _(3,19) -20 _(3,18) E	247044.146	140	-3.7	86	138 (9)	6.27 (0.16)	3.9 (-)
21 _(3,19) -20 _(3,18) A	247053.453	140	-3.7	86	138 (8)	6.61 (0.14)	3.9 (-)
CH₃CHO							
12 _(2,11) -11 _(2,10) E [v _t =1]	233048.516	285	-3.4	50	126 (9)	7.52 (0.11)	3.6 (0.3)
12 _(4,8) -11 _(4,7) E [v _t =2]	234707.132	487	-3.4	50	71 (10)	6.1 (0.3)	3.5 (-)
13 _(0,13) -12 _(0,12) E [v _t =2]	246169.217	461	-3.3	54	95 (8)	6.29 (0.12)	3.7 (0.3)
14 _(0,14) -13 _(1,13) A	247142.155	96	-4.2	58	85 (4)	7.16 (0.05)	3.1 (0.1)
14 _(0,14) -13 _(1,13) E	247341.332	96	-4.2	58	89 (3)	6.84 (0.05)	3.2 (0.1)
NH₂CHO							
11 _(4,8) -10 _(4,7)	233735.603	115	-3.1	69	174 (13)	7.66 (0.13)	4.3 (0.3)
11 _(4,7) -10 _(4,6)	233746.504	115	-3.1	69	165 (10)	7.58 (0.14)	4.5 (-)
11 _(3,9) -10 _(3,8)	233897.318	94	-3.1	69	157 (6)	7.76 (0.08)	4.41 (0.19)
11 _(3,8) -10 _(3,7)	234316.254	94	-3.1	69	160 (14)	7.48 (0.14)	4.5 (0.4)
12 _(0,12) -11 _(0,11)	247391.356	78	-3.0	75	133 (109)	7.37 (0.18)	4 (1)
12 _(2,10) -11 _(2,9) ^c	260189.848	92	-2.9	75	186 (5)	7.37 (-)	4 (-)
CH₃CH₂OH							
t-14 _(5,9) -14 _(4,10)	232928.499	120	-4.1	29	133 (10)	6.91 (0.14)	3.6 (0.3)
t-24 _(5,20) -24 _(4,21)	233208.521	285	-4.1	49	168 (12)	5.50 (0.17)	4.0 (-)
t-15 _(5,11) -15 _(4,12)	233215.475	132	-4.1	31	88 (9)	7.08 (0.14)	3.1 (0.3)
g-20 _(4,17) -20 _(3,17) [v _t =1-0]	233095.873	256	-4.4	41	103 (10)	6.03 (0.15)	3.7 (0.4)
t-13 _(5,8) -13 _(4,9)	233571.024	108	-4.2	27	106 (7)	7.24 (0.14)	3.5 (-)
t-14 _(5,10) -14 _(4,11)	233601.523	120	-4.1	29	113 (12)	6.89 (0.17)	3.7 (0.4)
g-9 _(4,5) -8 _(3,5) [v _t =0-1]	233714.281	114	-4.4	19	117 (9)	5.90 (0.14)	4.7 (0.4)

Table A.1. continued.

t-13 _(5,9) -13 _(4,10)	233951.119	108	-4.1	27	120 (6)	7.13 (0.08)	3.74 (0.19)
t-12 _(5,7) -12 _(4,8)	234051.119	97	-4.2	25	98 (8)	6.95 (0.19)	3.2 (0.3)
t-12 _(5,8) -12 _(4,9)	234255.161	97	-4.2	25	148 (5)	7.61 (0.07)	4.26 (0.17)
g-15 _(0,15) -14 _(1,13) [$v_t=0-1$]	234360.555	158	-4.4	31	115 (9)	6.31 (0.09)	3.0 (0.2)
t-11 _(5,6) -11 _(4,7)	234406.451	87	-4.2	23	88 (11)	6.77 (0.17)	3.2 (0.4)
t-31 _(3,28) -31 _(2,29)	234481.343	437	-4.1	63	45 (6)	7.0 (-)	3.2 (0.5)
t-11 _(5,7) -11 _(4,8)	234509.565	87	-4.2	23	148 (6)	7.34 (0.07)	3.55 (0.16)
t-25 _(5,21) -25 _(4,22)	234523.893	306	-4.1	51	143 (6)	7.37 (0.08)	3.89 (0.19)
t-10 _(5,5) -10 _(4,6)	234666.273	78	-4.2	21	108 (10)	6.99 (0.17)	3.7 (0.4)
t-10 _(5,6) -10 _(4,7)	234714.571	78	-4.2	21	98 (10)	6.4 (-)	3.1 (0.4)
t-23 _(1,22) -23 _(0,23)	234725.600	233	-3.8	47	93 (11)	6.3 (0.3)	4.4 (0.6)
g-14 _(3,11) -13 _(3,10) [$v_t=0-0$]	246414.762	156	-3.9	29	110 (10)	6.88 (0.15)	3.5 (0.4)
CH ₂ OHCHO							
26 _(10,16) -26 _(9,17)	233587.449	256	-3.7	53	68 (9)	7.1 (0.2)	3.0 (-)
26 _(10,17) -26 _(9,18)	233709.657	256	-3.7	53	72 (6)	7.12 (0.11)	3.0 (0.3)
38 _(11,27) -38 _(10,28)	234554.566	489	-3.7	77	50 (4)	6.72 (0.14)	3.0 (-)
25 _(10,15) -25 _(9,16)	234704.065	242	-3.7	77	65 (11)	6.5 (0.2)	3.3 (0.6)
34 _(4,30) -34 _(3,31)	246395.021	344	-3.8	69	94 (10)	7.98 (0.17)	4.9 (0.5)
34 _(5,30) -34 _(4,31)	246605.634	344	-3.8	69	90 (7)	7.32 (0.15)	4.4 (0.4)
30 _(2,28) -30 _(1,29)	246773.215	253	-4.0	61	70 (4)	7.01 (0.09)	3.7 (0.2)
30 _(3,28) -30 _(2,29)	246778.410	253	-4.0	61	60 (6)	7.27 (0.16)	3.9 (0.4)
36 _(11,26) -36 _(10,27)	246852.728	446	-3.6	73	81 (7)	6.83 (0.10)	3.3 (0.2)
32 _(3,29) -32 _(2,30)	247285.434	297	-3.9	65	92 (9)	6.64 (-)	3.5 (-)
32 _(4,29) -32 _(3,30)	247323.158	297	-3.9	65	50 (11)	6.73 (-)	3.5 (-)

^aSpectroscopic parameters of CH₃OH (Xu et al. 2008) and CH₂OHCHO (Johnson et al. 2013; Collier et al. 2021) are retrieved from the CDMS molecular database (Endres et al. 2016, Cologne Database for Molecular Spectroscopy), and the ones of HCOOCH₃ (Ilyushin et al. 2009), CH₃CHO (Kleiner et al. 1996), NH₂CHO (Kurland & Wilson 2004; Kukolich & Nelson 1971; Kirchhoff & Johnson 1973; Johnson et al. 2009; Costain & Dowling 1960), and CH₃CH₂OH (Pearson et al. 2008) from the JPL molecular database (Pickett et al. 1998; Drouin 2017, Jet Propulsion Laboratory). ^bResults of the Gaussian fit algorithm in CARTA. Note that the spectral resolution is 1.4 km s⁻¹. In round parentheses are reported the uncertainties on the fitted quantities. The dash symbol indicates that the quantity has been fixed during the line fitting procedure. ^c Refers to the transition detected in the narrow SPW centred at 260 GHz.

Appendix B: Image plane fit results

Table B.1. Image plane Gaussian fitted parameters for selected transitions.

Transition	E _u [K]	R.A. [h: m: s]	Dec. [° : ' : "]	θ_M [mas]	θ_m [mas]	P.A. [°]
CH ₃ OH						
10 _(3,7) -11 _(2,9) E	191	03:29:10.431 (0.002")	+31.13.32.023 (0.002")	331 (7)	224 (6)	130 (3)
18 _(3,15) -17 _(4,14) A	447	03:29:10.4306 (0.0013")	+31.13.32.0178 (0.0014")	257 (6)	207 (8)	107 (6)
4 _(2,3) -5 _(1,4) A	61	03:29:10.431 (0.002")	+31.13.32.022 (0.002")	351 (8)	232 (7)	129 (3)
5 _(4,2) -6 _(3,3) E	123	03:29:10.431 (0.002")	+31.13.32.023 (0.002")	315 (8)	229 (8)	121 (4)
16 _(-2,15) -15 _(-3,13) E	338	03:29:10.430 (0.002")	+31.13.32.0118 (0.0019")	302 (7)	224 (6)	122 (4)
4 _(2,2) -5 _(1,5) A	61	03:29:10.430 (0.003")	+31.13.32.019 (0.003")	353 (9)	239 (6)	130 (3)
18 _(3,15) -18 _(2,16) A	447	03:29:10.430 (0.002")	+31.13.32.017 (0.002")	310 (8)	224 (6)	125 (4)
HCOOCH ₃						
19 _{4,16} -18 _{4,15} A	123	03:29:10.432 (0.002")	+31.13.32.010 (0.002")	322 (8)	231 (8)	118 (4)
18 _{4,14} -17 _{4,13} E	114	03:29:10.432 (0.002")	+31.13.32.010 (0.002")	313 (8)	229 (8)	117 (4)
19 _(11,9) -18 _(11,8) E	193	03:29:10.432 (0.003")	+31.13.32.010 (0.003")	277 (11)	220 (13)	105 (10)
20 _(13,8) -19 _(13,7) E	236	03:29:10.431 (0.003")	+31.13.32.004 (0.003")	258 (13)	204 (13)	107 (11)
20 _(6,15) -19 _(6,14) A [$v=1$]	336	03:29:10.431 (0.004")	+31.13.32.004 (0.004")	247 (16)	204 (16)	106 (17)
CH ₃ CHO						
12 _(2,11) -11 _(2,10) E [$v_t=1$]	285	03:29:10.4311 (0.0011")	+31.13.32.0064 (0.0014")	206 (4)	182 (6)	91 (12)
12 _(4,8) -11 _(4,7) E [$v_t=2$]	487	03:29:10.4312 (0.0018")	+31.13.31.998 (0.002")	186 (11)	165 (13)	52 (26)
13 _(0,13) -12 _(0,12) E [$v_t=2$]	461	03:29:10.4303 (0.0016")	+31.13.31.9957 (0.0018")	160 (8)	157 (9)	73 (75)
14 _(0,14) -13 _(1,13) A	96	03:29:10.431 (0.003")	+31.13.31.999 (0.002")	249 (10)	192 (11)	95 (9)
NH ₂ CHO						

Table B.1. continued.

11 _(4,7) -10 _(4,6)	115	03:29:10.4306 (0.0008")	+31.13.32.0060 (0.0012")	165 (6)	153 (5)	154 (19)
11 _(3,9) -10 _(3,8)	94	03:29:10.4308 (0.0008")	+31.13.32.0090 (0.0012")	165 (6)	139 (5)	149 (9)
12 _(0,12) -11 _(0,11)	78	03:29:10.4303 (0.0010")	+31.13.32.0017 (0.0012")	158 (5)	136 (3)	148 (10)
CH₃CH₂OH						
g-20 _(4,17) -20 _(3,17) [$v_t=1-0$]	256	03:29:10.4308 (0.0012")	+31.13.32.0075 (0.0017")	185 (8)	165 (8)	36 (16)
t-13 _(5,9) -13 _(4,10)	108	03:29:10.4312 (0.0014")	+31.13.32.0128 (0.0016")	210 (6)	179 (8)	80 (11)
t-12 _(5,8) -12 _(4,9)	97	03:29:10.4311 (0.0011")	+31.13.32.0078 (0.0013")	207 (5)	175 (7)	80 (9)
t-25 _(5,21) -25 _(4,22)	306	03:29:10.4310 (0.0009")	+31.13.32.0081 (0.0013")	169 (6)	162 (6)	44 (37)
g-14 _(3,11) -13 _(3,10) [$v_t=0-0$]	156	03:29:10.4302 (0.0018")	+31.13.32.0064 (0.0018")	200 (9)	169 (10)	83 (11)
CH₂OHCHO						
26 _(10,17) -26 _(9,18)	256	03:29:10.4315 (0.0013")	+31.13.32.001 (0.002")	154 (10)	144 (8)	16 (79)
38 _(11,27) -38 _(10,28)	489	03:29:10.4318 (0.0017")	+31.13.32.004 (0.003")	169 (12)	155 (4)	13 (89)
34 _(5,30) -34 _(4,31)	344	03:29:10.4304 (0.0019")	+31.13.32.001 (0.002")	153 (9)	139 (7)	158 (51)
30 _(2,28) -30 _(1,29)	253	03:29:10.431 (0.002")	+31.13.31.995 (0.003")	149 (14)	129 (17)	30 (37)
36 _(11,26) -36 _(10,27)	446	03:29:10.4308 (0.0018")	+31.13.31.997 (0.003")	143 (12)	115 (13)	16 (19)

Each species transitions are listed in order of increasing rest-frame frequency. Uncertainties are indicated in round parentheses.

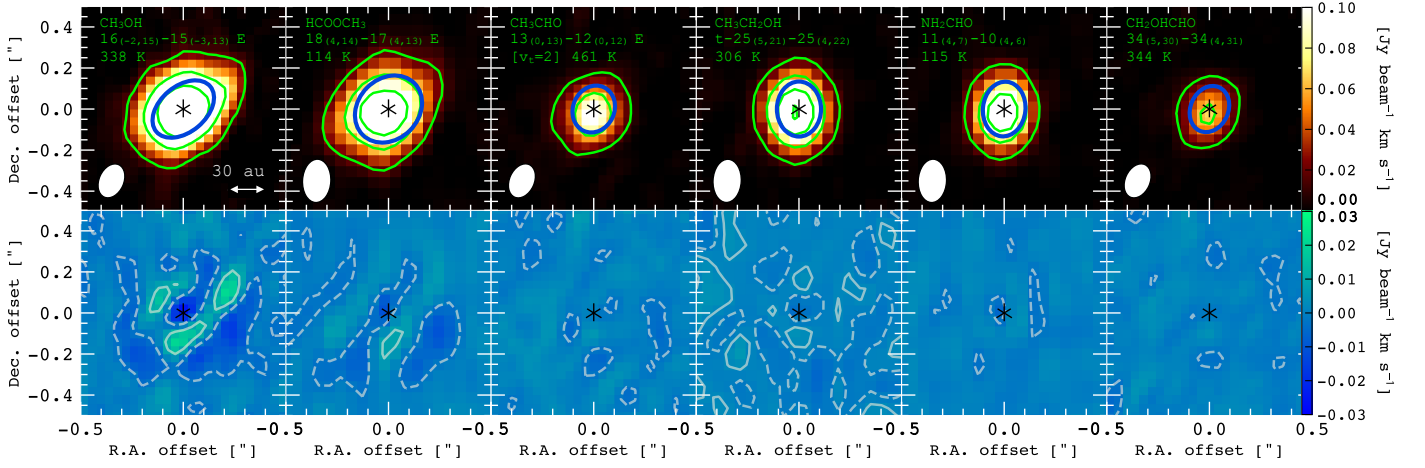


Fig. B.1. Examples of integrated intensity maps (*left*) and image fit residuals (*right*) in colour scale of the isolated iCOMs lines from which the emission size has been extracted. *Left*: First contours and steps are respectively 5σ and 20σ . The black marker corresponds to the centroid of the map. The blue solid line is the fitted Gaussian ellipse convolved with the beam. The synthesized beams refer to S1 ($0''.21 \times 0''.14$, -3°) and S2 ($0''.17 \times 0''.12$, -28°). *Right*: Dashed and solid contours are respectively the -1σ and 3σ levels of the residual map. The black marker corresponds to the centroid of the map.

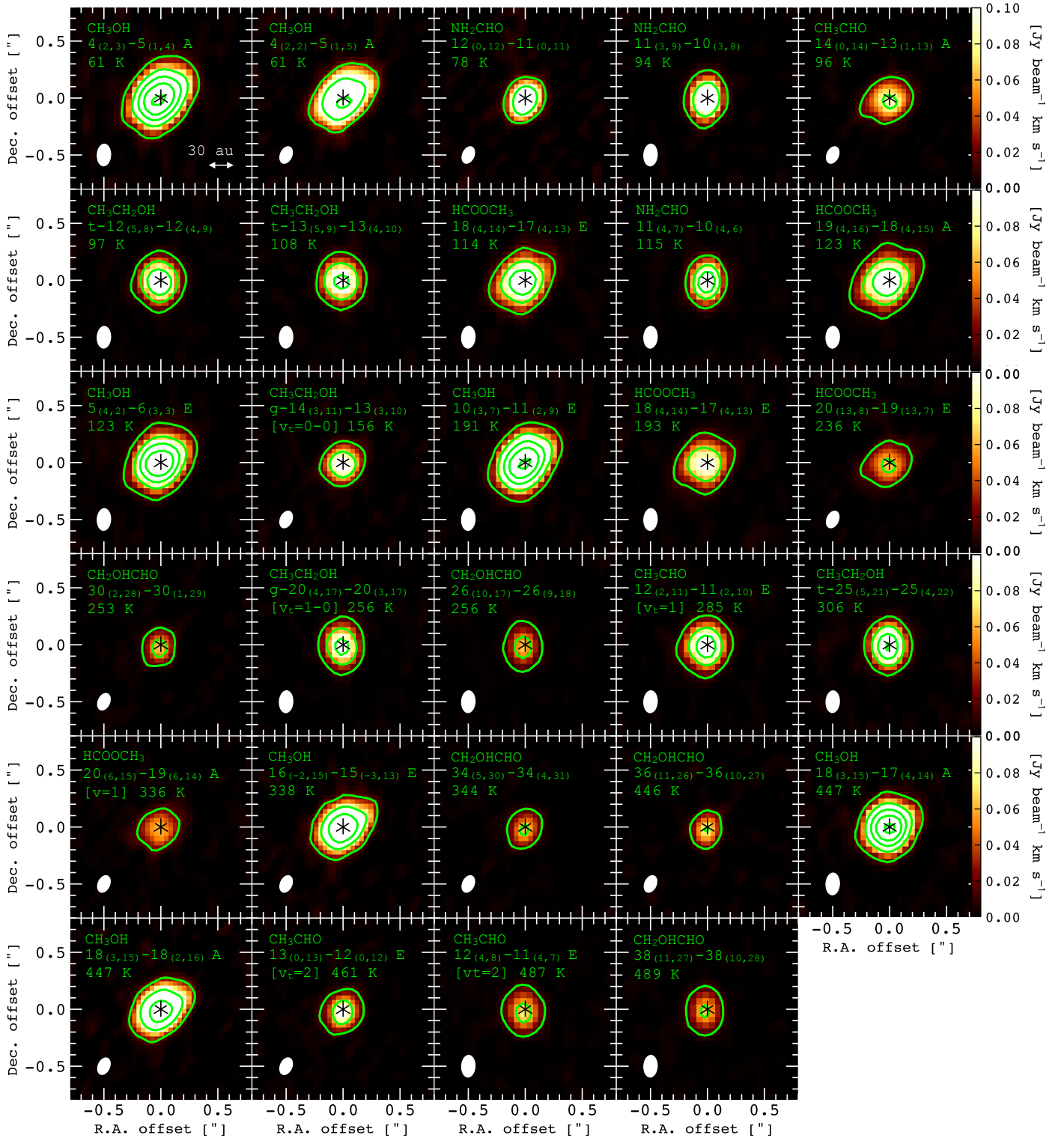


Fig. B.2. Integrated intensity maps in colour scale and green contours of the isolated iCOMs lines from which the emission size has been extracted. The maps are plotted in order of increasing upper-state energy. First contours and steps are respectively 5σ and 20σ . The black marker corresponds to the centroid of the map. The synthesized beams refer to S1 ($0''.21 \times 0''.14, -3^\circ$) and S2 ($0''.17 \times 0''.12, -28^\circ$).

Appendix C: Non-LTE LVG Analysis for CH₃OH

Since methanol (CH₃OH) is known to be very abundant in this source (see e.g., De Simone et al. 2020a) and optically-thick, to complement and check the analysis made with the LTE and optically-thin line assumptions, we performed a non-LTE analysis using a Large Velocity Gradient (LVG) code (Ceccarelli et al. 2003). We could therefore derive the physical properties of the gas emitting CH₃OH, namely gas temperature, density and column density, and the optical depth of the transitions. We used the collisional coefficients of both A-type and E-type of CH₃OH with para-H₂, computed by Rabli & Flower (2010) between 10 and 200 K for the first 256 levels and provided by the BASecOL database (Dubernet et al. 2013). Note that, given that the coefficients are available only for transition with J up to 15 and computed for temperatures up to 200 K, we used the transitions that in this work have E_u less than 200 K. For this purpose we added the transition identified in the narrow SPW centered at 244 GHz, identified as 5_(1,3) – 4_(1,3) A with the following spectroscopic and Gaussian parameters: E_u = 50 K; Log₁₀A_{ul} = -4.7; g_u = 44; W = 340 ± 10 K km s⁻¹; V_{peak} = 6.74 ± 0.08 km s⁻¹; FWHM = 5.8 ± 0.2 km s⁻¹. We assumed a spherical geometry to compute the line escape probability, the CH₃OH-A/CH₃OH-E ratio equal to 1, and the H₂ ortho-to-para ratio equal to 3. We ran a large rid of models (~13,000) covering the frequency of the observed CH₃OH lines, a total (A-type plus E-type) column density N_{CH₃OH} from 10¹⁶ to 4 × 10¹⁹ cm⁻², a gas density n_{H₂} from 10⁶ to 2 × 10⁸ cm⁻³, both sampled in logarithmic scale, and a gas temperature T from 80 to 190 K, sampled in linear scale. We then simultaneously fitted the measured CH₃OH-A and CH₃OH-E line intensities via comparison with those simulated by the LVG model, leaving N_{CH₃OH}, n_{H₂}, and T as free parameters. Following the observations, we assumed a source size of 0''.3 to compute the filling factor, a linewidth equal to 4.5 km s⁻¹, and we included the calibration/continuum subtraction uncertainty (20%) in the observed intensities.

The chi-square best fit is obtained for a total CH₃OH column density of 2 × 10¹⁸ cm⁻², a gas temperature of 100 K and gas density of 2 × 10⁶ cm⁻³, with reduced chi-square $\tilde{\chi}^2 = 0.6$. Finally, we corrected the intensities for the foreground dust absorption. In this case, the best fit is obtained for a total CH₃OH column density of 4 × 10¹⁸ cm⁻², a gas temperature of 150 K and gas density of 5 × 10⁶ cm⁻³, with reduced chi-square $\tilde{\chi}^2 = 0.3$. The results do not change assuming a linewidth ±0.5 km s⁻¹ with respect to the chosen one. Figure 3 shows the density-temperature χ^2 surface of the N_{CH₃OH} best fit. The fit results in the 1σ confidence range are reported in Tab. 1.

Appendix D: LTE Population Diagram analysis

We performed a population diagram analysis on methyl formate (HCOOCH₃), ethanol (CH₃CH₂OH), and glycolaldehyde (CH₂OHCHO) to correct rotational temperature T_{rot} and total column density N_{tot} for the line optical depth (τ), following the prescription of Goldsmith & Langer (1999). The optical depth of a transition can be written as:

$$\tau = \frac{c^3}{8\pi\nu_0^3} \frac{A_{ul}}{\Delta V / (2\sqrt{2} \ln 2)} \frac{N_u}{g_u} \left(e^{h\nu_0/kT_{rot}} - 1 \right) \quad (D.1)$$

where

$$N_u = W \times \frac{8\pi k\nu_0^2}{h c^3 A_{ul} f f} \times C_\tau. \quad (D.2)$$

In the above, *c* is the speed of light, ν_0 the rest-frame line frequency, A_{ul} the Einstein coefficient for spontaneous emission, ΔV the line profile FWHM (derived by fitting the line with a gaussian profile), g_u the statistical weight of the upper state, E_u the upper-state energy of the transition, *h* and *k* respectively the Planck and the Boltzmann constants, *W* the velocity-integrated line intensity, and *ff* the beam filling factor, defined as: $ff = \theta_{source}^2 / (\theta_{source}^2 + \theta_{beam}^2)$ (e.g. Mangum & Shirley 2015). θ_{beam} is the synthesized beam of the observations. All units refer to the cgs system.

Finally, C_τ is the optical depth correction factor:

$$C_\tau = \frac{1 - e^{-\tau}}{\tau} \quad (D.3)$$

This factor indicates how much the upper level populations (N_u) are underestimated due to the line opacity. When the line is optically-thin, C_τ is equal to unity.

For a molecule in LTE, all excitation temperatures are the same, and the population of each level is given by:

$$\ln\left(\frac{N_u}{g_u}\right) = \ln\left(\frac{N_{tot}}{Q(T_{rot})}\right) - \frac{E_u}{kT_{rot}} \quad (D.4)$$

where N_{tot} the species total column density, and Q(T_{rot}) the partition function at the rotational temperature T_{rot} of the species.

We created a 2D parameter space grid in rotational temperature (50 values between 50 and 500 K), and in total column density (50 values between 1 × 10¹⁶ and 5 × 10¹⁹ cm⁻²) at fixed source size θ_{source} (see Tab. 1). For each set of T_{rot} and N_{tot} we computed the model upper state column densities N_{u, model} using equation D.3, as well as the line opacity τ (Eq. D.1) and the resulting C_τ (Eq. D.3). Then we retrieved the corrected upper state column densities N_{u, corr} using Eq. D.2, in which the observed velocity-integrated line intensities are corrected for the beam dilution and the opacity factor. Finally, we performed a chi-square minimization test comparing N_{u, corr} and N_{u, model}:

$$\tilde{\chi}^2 = \frac{1}{N-3} \sum_{i=1}^N \frac{\ln(N_{u,corr,i}/g_{u,i}) - \ln(N_{u,model,i}/g_{u,i})}{\sigma_i^2} \quad (D.5)$$

Here, *N* is the number of observed lines, while σ is the observed error on ln(N_u/g_u), calculated as:

$$\sigma = \frac{\sqrt{(\Delta W)^2 + \sigma_f^2}}{W} \quad (D.6)$$

where ΔW is the error on the fitted line intensities (see Tab. A.1), and σ_f is the absolute flux calibration error, that we fixed as 20% of *W*. In Figs. 4 and D.1 respectively, we report the results of this analysis accounting respectively for all transitions and the low excitation ones (E_u < 300 K) only.

Accounting solely for lines with E_u ≤ 300 K (see Tab. D.1), T_{rot} and N_{tot} are strongly degenerate in the case of HCOOCH₃ and CH₂OHCHO, and less degenerate for CH₃CH₂OH. The resulting minimum $\tilde{\chi}^2$ is 0.6 (HCOOCH₃), 0.4 (CH₃CH₂OH), and 0.6 (CH₂OHCHO). We could extract only a lower limit on the temperature for HCOOCH₃, and a lower limit on the total column density for CH₃CH₂OH and CH₂OHCHO.

The inclusion of high excitation lines (Fig. 4) helps closing the $\tilde{\chi}^2$ contours within the investigated parameter space, and to attenuate the degeneracy between T_{rot}, N_{tot} and τ. The minimum $\tilde{\chi}^2$ in this case is 1.0 (HCOOCH₃), 0.9 (CH₃CH₂OH), and 0.5 (CH₂OHCHO).

Accounting for a 50% millimeter dust obscuration factor⁷ on the velocity-integrated line intensities, the effect is to increase the best-fit temperature range by 50-100 K within error bars, and increase the total column density by a factor of about 1.6 (2.2 for CH₃CH₂OH). The best-fit χ^2 is 0.6 (HCOOCH₃), 0.6 (CH₃CH₂OH), and 0.6 (CH₂OHCHO) for $E_u < 300$ K, and 1.4 (HCOOCH₃), 1.3 (CH₃CH₂OH), and 0.5 (CH₂OHCHO) using all lines. The effect on the line optical depth is to change the average line opacity by 0.4 dex ($E_u < 300$ K) and 0.1 dex (all lines).

Table D.1. 1σ confidence level results of the population diagram analysis with $E_u < 300$ K.

Species	No dust obscuration		With dust obscuration	
	T_{rot} [K]	N_{tot} [cm ⁻²]	T_{rot} [K]	N_{tot} [cm ⁻²]
HCOOCH ₃	>110	$0.4\text{-}1.5 \times 10^{18}$	>170	$0.8\text{-}2.4 \times 10^{18}$
CH ₃ CH ₂ OH	130-240	$>8 \times 10^{17}$	190-400	$>1.8 \times 10^{18}$
CH ₂ OHCHO	110-480	$>2 \times 10^{17}$	>160	$>3 \times 10^{17}$

The source size derived from image fitting is assumed for each species (see Sec. 3.1).

⁷ 30%, according to De Simone et al. (2020a), for the sample of CH₂OHCHO lines from Taquet et al. (2015).

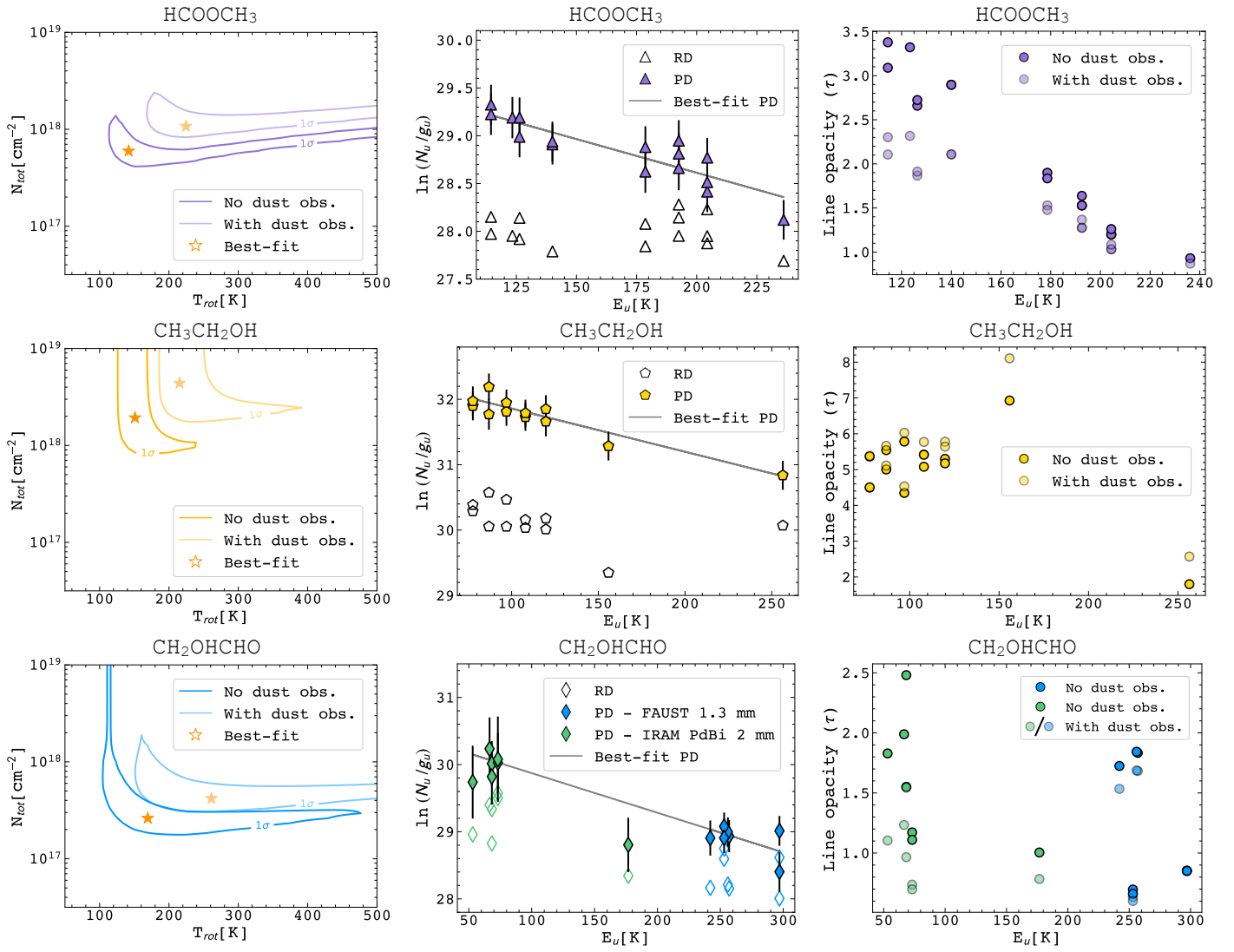


Fig. D.1. Same as Fig. 4 for lines with $E_{\text{u}} < 300$ K.

Appendix E: Additional notes and results

Figure E.1 shows the rotational diagram of CH_3CHO computed using all lines (see Tab. A.1), and correcting for the derived source size of $0''.20$. Shaded data points and solid line take into account the mm dust obscuration (see Sect. 4.1). The best-fit results in both cases are reported in Tab. 1.

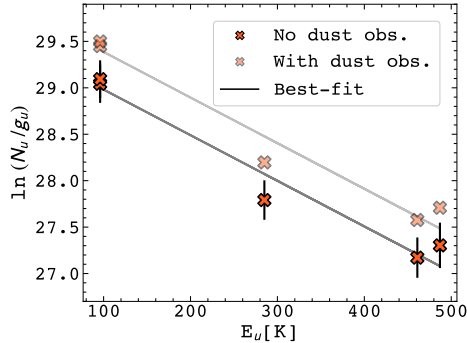


Fig. E.1. Rotational diagram (RD) of CH_3CHO . The solid gray line is the best-fit to the data points with (*shaded*) and without (*full color*) mm dust obscuration factor. The upper-state column densities are corrected for beam dilution.

Figure E.2 shows the gas radial temperature profile of IRAS 4A2 obtained from the population diagram analysis of HCOOCH_3 , $\text{CH}_3\text{CH}_2\text{OH}$, and CH_2OHCHO below 300 K, and the non-LTE LVG analysis of CH_3OH . CH_3CHO and NH_2CHO are here not reported, as it was not possible to perform a conservative line analysis or obtain an independent estimate of the gas temperature, respectively. The grey dotted line refers to the best-fit to the data points of the top panel in Fig. 5.

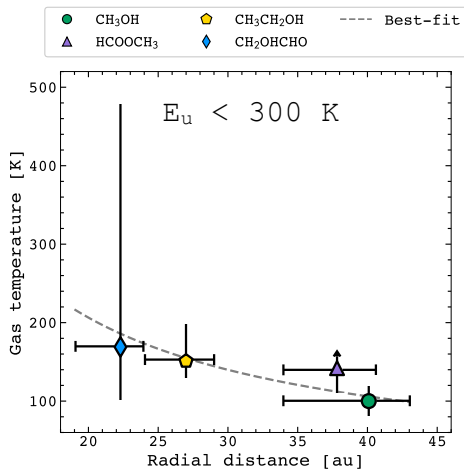


Fig. E.2. Same as Fig. 5 from iCOMs transitions with $E_u < 300$ K. The arrow indicates a lower limit on the temperature. The grey dotted line is the best-fit to the data points in the top panel of Fig. 5).